Universität Hamburg
DER FORSCHUNG | DER LEHRE | DER BILDUNG

Studying the Influence of the PMT Charge Spectrum on Energy Resolution at the JUNO Detector

Studien zum Einfluss des PMT-Ladungsspektrums auf die Energieauflösung am JUNO-Detektor

Julius Römer

June 2019

Universität Hamburg

1. reviewer: Dr. Björn Sönke Wonsak
2. reviewer: Prof. Dr. Caren Hagner

Abstract

The Jiangmen Underground Neutrino Observatory (JUNO) aims to determine the mass ordering of the neutrino mass eigenstates. In order to fulfill its primary target, an energy resolution of 3 % at 1 MeV must be reached. JUNO is a liquid scintillator experiment with 20 kton linear alkyl benzene (LAB) and 45,000 PhotoMultiplier Tubes (PMTs). Tests determined that the PMTs used for enery measurements have a broad charge spectrum. The influence of the charge distribution on the energy resolution is analysed with a Toy-Monte-Carlo simulation. A likelihood method to improve energy resolution is tested as well. It was determined that the long tail of the charge distribution alone worsens the energy resolution by $\sim 0.4\,\%$ at 1 MeV. The likelihood method showed nearly maximum energy resolution.

Zusammenfassung

Das Ziel vom Jiangmen Underground Neutrino Observatory (JUNO) ist es, die Massenordnung der Neutrino Masseneigenzustände zu bestimmen. Dafür muss eine Energieauflösung von 3 % bei 1 MeV erreicht werden. Dazu ist JUNO mit 20 kilotonnen Linear Alkyl Benzen (LAB) Flüssigszintillator und 45,000 PhotoMultiplier Tubes (PMTs) ausgestattet. Es hat sich herausgestellt, dass die PMTs eine breite Ladungsverteilung besitzen. Deren Einfluss auf die Energieauflösung wird mit Hilfe einer Toy-Monte-Carlo Simulation überprüft. Zudem wird eine Likelihood Methode getestet, die die Energieauflösung verbessern soll. Es hat sich herausgestellt, dass allein das ausgedehnte Ende der Ladungsverteilung eine Verschlechterung von 0.4% bei 1 MeV mit sich bringt. Die Likelihood Methode erzielte die nahezu bestmögliche Energieauflösung.

Contents

Introduction

Neutrinos make up a special field in the scope of elementary particle physics. With their tiny, still undisclosed masses and small cross sections, detecting these leptons is a challenging task. However, neutrino experiments do not only yield knowledge on particle physics, but also on geothermal activity, the sun, stellar collapse and possibly dark matter.

In the Standard Model of particle physics it was proposed that neutrinos are massless. Another neutrino phenomena has shown otherwise: Neutrinos transition into another flavour eigenstate over time, which was first discovered in the Homestake experiment, where a deficit of electron neutrinos in the solar neutrino flux has been observed. The missing neutrinos were not actually absent, they just appeared in a different flavour. This neutrino oscillation is heavily dependant on the square mass differences of the mass eigenstates which shows that the neutrino mass cannot be zero. Furthermore, the absolute mass differences have been resolved, although the absolute neutrino masses are still unknown. This leaves us with two possibilities for the ordering of the square mass differences of the mass eigenstates, also known as mass hierarchy or mass ordering.

Many neutrino experiments revolve around questions on neutrino mass and oscillation. The Jiangmen Underground Neutrino Observatory (JUNO) is one of them. It is a spherical detector with a diameter of 35 m holding 20 kton of Liquid Scintillator (LS). Passing particles create light signals in the LS that will be counted by 45,000 Photo Multiplier Tubes (PMTs). The Central Detector (CD) is surrounded by a pure water tank and located underground with a total overburden of 700 m to shield the detector from atmospheric muons. This is needed to detect reactor neutrinos generated in two 53 km distant nuclear power plants with sufficient certainty.

Primarily, JUNO aims to determine the mass ordering by measuring the oscillation pattern of the reactor neutrinos. In order to do so, an energy resolution of 3 % at 1 MeV is needed. This is heavily dependant on the number of photons created in the LS and on the precise detection of photons by the PMTs. Tests show that the majority of used PMTs possess a broad charge distribution for single photon hits. This reduces the possibility of reliable energy reconstruction.

In the scope of this thesis, the influence of the charge distribution on the energy resolution at JUNO will be examined. Different methods of estimating the energy will be

tested, including a likelihood method that combines several information and is expected to improve the energy resolution. To do so, a Toy Monte Carlo simulation of the JUNO detector and the resulting signals at the PMTs will be conducted.

The underlying neutrino physics including neutrino oscillation is discussed in chapter 1. Chapter 2 outlines the basic setup of JUNO and details relevant for this thesis. The Toy Monte Carlo simulation is explained in chapter 3. The results of the simulation are presented in chapter 4, a summary and an outlook is provided in chapter 5.

1 Neutrino Physics

In this chapter, the physics and interactions of neutrinos are explained. At first, the sources and the discovery of the neutrino are outlined. In section 1.1 the standard model, including the neutrino types $\nu_e, \bar{\nu}_e, \nu_\mu, \bar{\nu}_\mu, \nu_\tau, \bar{\nu}_\tau$ is explained. Section 1.2 outlines the phenomena of neutrino oscillation, which is the foundation for the JUNO experiment.

Neutrinos are elementary spin-$\frac{1}{2}$ particles. They are very light even compared to other elementary particles and carry no electric charge. These attributes result in low probabilities of neutrinos to interact with matter. Therefore, neutrinos can travel through a vast amount of matter and are very difficult to detect. However, neutrinos have various sources and can yield information on numerous phenomena in the universe. Neutrinos are commonly distinct through their sources:

- Geo-neutrinos ($\nu_e, \bar{\nu}_e$) originate from natural β-decay in the earth's interior. The isotopes ^{238}U, ^{232}Th, and ^{40}K are the main contributors to both geo-neutrino flux and radiogenic heat in the earth's crust and mantles [2]. Thus, analyzing geo-neutrinos will improve models of the earth.

- Reactor neutrinos ($\bar{\nu}_e$) are anti-electron-neutrinos from β-decay in nuclear power plants. One expects about $2 \times 10^{20} \, \nu/s$ emitted isotropically from a reactor with 1 GW thermal power [3]. Reactor neutrinos are measured in JUNO to achieve its main goal. More information on reactor neutrinos in JUNO is provided in chapter 2.

- Neutrinos can also be produced in particle accelerator experiments ($\nu_\mu, \bar{\nu}_\mu$). They are produced in the decay of high energy mesons [30] and are also used for neutrino oscillation experiments [27].

- Atmospheric neutrinos ($\nu_e, \bar{\nu}_e, \nu_\mu, \bar{\nu}_\mu$) are produced when cosmic particles (mostly protons) collide with nuclei in earth's atmosphere. They then form mesons, which decay and result in neutrinos along with other particles [30].

- Solar neutrinos (ν_e) originate from nuclear fusion of hydrogen in the sun. Since they leave the sun without interacting with matter, solar neutrinos provide real-time insights to processes inside the sun. More on solar neutrinos can be found in section 1.2.

- 99% of the energy produced in a supernova core-collapse is carried away by neutrinos [32]. Studying these supernova neutrinos ($\nu_e, \bar{\nu}_e, \nu_\mu, \bar{\nu}_\mu, \nu_\tau, \bar{\nu}_\tau$) will improve the understanding of stellar collapses. A nearby supernova burst may be seen because of the immense neutrino flux, but they are very rare. However, from many supernova bursts of the past, a diffuse supernova neutrino background (DSNB) should be present. The DSNB has not been observed yet [9].

- The rare high energy cosmic neutrinos ($\nu_e, \bar{\nu}_e, \nu_\mu, \bar{\nu}_\mu$) originate from the decay of mesons that are products of collisions of high energy particles with nucleons or photons [30]. Even though these neutrinos are very rare, the IceCube experiment was able to backtrack one of these to a blazar in 2018 [15].

- Cosmic background neutrinos ($\nu_e, \bar{\nu}_e, \nu_\mu, \bar{\nu}_\mu, \nu_\tau, \bar{\nu}_\tau$) are remnants from a neutrino gas that formed shortly after the big bang. They possess little energy $\langle E \rangle = 5.3 \cdot 10^{-4}$ eV and are thus difficult to detect. These neutrinos are candidates for a portion of the dark matter [30]. Determining the absolute neutrino masses is crucial for further propositions regarding this theory.

Neutrino physics was born in 1914, when James Chadwick examined the β-decay [37]

$$n \rightarrow p + e^- + \bar{\nu}_e \,, \tag{1.1}$$

where n is the neutron which was not detected until 1932, p the proton, e^- the electron and finally $\bar{\nu}_e$, the electron-antineutrino.

Chadwick measured a continuous energy spectrum of the electron below the total released energy, which was the expected value, shown in fig. 1.1. This can be explained if the measured electron is the product of a secondary process, which would broaden the energy spectrum. However, it was determined that the electron is, in fact, the primary electron. A primary electron with continuous energy distribution can be explained by a violation of energy conservation or by another yet undiscovered product. In December 1930, Wolfgang Pauli then proposed the solution: A new spin-$\frac{1}{2}$ particle, at first called neutron. The additional particle, later known as the neutrino, carries the missing energy.

The discovery of the neutrino finally took place in 1956. Frederick Reines and Clyde L. Cowan Jr. measured characteristic signals from the inverse β-decay (IBD)

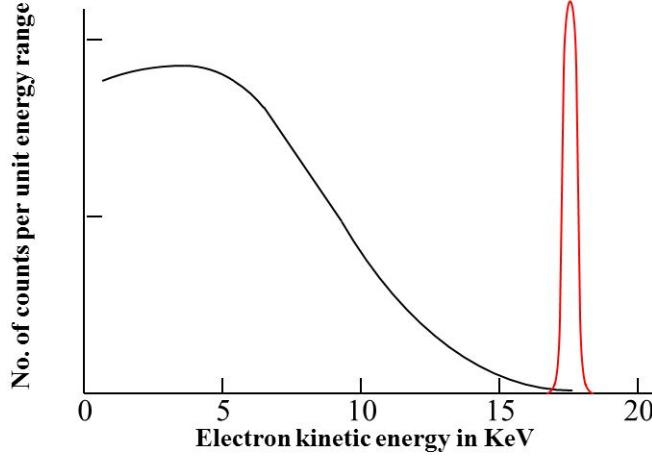$$\bar{\nu}_e + p \longrightarrow e^+ + n \tag{1.2}$$

Figure 1.1: The energy spectrum of the resulting electron from β-decay [18]. The black curve shows the measured spectrum, the red peak shows the expected electron energy.

induced by electron-antineutrinos coming from the β-decay in nuclear power plants. This method is also the main detection channel in JUNO and will be discussed in section 2.3.

1.1 Standard Model

The Standard Model (SM) delivers classification of elementary particles and their interactions via three of the four fundamental forces: Strong, weak and electromagnetic interaction with gravity being ignored. The theoretical foundation is the requirement of local symmetry of the gauge group [29]

$$\mathrm{SU}(3)_c \times \mathrm{SU}(2)_L \times \mathrm{U}(1)_\gamma \,. \tag{1.3}$$

The SM includes fermions with spin $S = \frac{1}{2}$, which are separated into quarks and fermions, the Higgs boson ($S = 0$) and the gauge bosons ($S = 1$). The SM also includes all antiparticles to the fermions. Antiparticles share almost all physical attributes with their counterparts, but carry opposite charges [33].
The Higgs boson, discovered in 2012, takes a special place in the SM theory. Interaction with the Higgs boson is responsible for the masses of fermions [33]. In the following, the masses of particles are expressed in natural units $c = 1$, where c is the speed of light.

In the SM, or more precisely in Quantum Field Theory (QFT), the forces between particles are described as the exchange of Spin-1 particles, the gauge bosons. An overview of gauge bosons and their corresponding forces is given in table 1.1. Electromagnetic force is discussed within the scope of Quantum Electro Dynamics (QED) as the exchange of

Table 1.1: The gauge bosons with their corresponding force, charge and mass [7].

Name, Symbol	**Photon, γ**	**W-Boson, $W^\pm$**	**Z-Boson, Z^0**	**Gluon, g**
Force	Electromagnetic	Weak	Weak	Strong
Mass	0	80.4 GeV	91.2 GeV	0
Electric charge [e]	0	± 1	0	0

Table 1.2: The Quarks in the SM with their corresponding mass and charge [7]

Generation	1st	2nd	3rd
Name	**up**	**charm**	**top**
Symbol	u	c	t
Charge [e]	$+\frac{2}{3}$	$+\frac{2}{3}$	$+\frac{2}{3}$
Mass	2.4 MeV	1.27 GeV	171.2 GeV
Name	**down**	**strange**	**bottom**
Symbol	d	s	b
Charge [e]	$-\frac{1}{3}$	$-\frac{1}{3}$	$-\frac{1}{3}$
Mass	4.8 MeV	1.04 GeV	4.2 GeV

massless photons (γ) between particles that carry an electric charge. This corresponds to the local symmetry of the group $U(1)_\gamma$ in eq. (1.3). Gauge bosons of the weak interactions are the W^+, W^- bosons with mass $m = 80.5$ GeV and the Z^0 boson with $m = 91.2$ GeV. The W-bosons carry the elementary electric charge $\pm e$. All fermions possess isospin, the charge of weak interaction, and thus interact via the weak force ($SU(2)_L$ in eq. (1.3)). All particles with electric charge interact electromagnetically and only the quarks additionally interact via the gauge bosons of the strong interaction, the gluons. Strong interaction is described in Quantum Chromo Dynamics (QCD). The quarks carry a color charge (r, g or b), which results in 8 flavors of gluons under local symmetry of $SU(3)_C$ [33]. Gluons are massless and have first been discovered at DESY in Hamburg [17].

The quarks (abbreviated as q) form three generations with increasing masses: The first generation is the up-quark u with electric charge $Q = +\frac{2}{3}e$ and down-quark d with $Q = -\frac{1}{3}e$ which make up protons p (uud) and neutrons n (udd). Other quarks are strange, charm, top and bottom (s, c, t, b). An overview of quarks and their attributes is given in table 1.2. Quarks only appear in bound states, the hadrons, and never as free particles. Hadrons can be baryons (qqq or $\bar{q}\bar{q}\bar{q}$) or mesons ($q\bar{q}$). An example for the baryons is the proton p (uud) and for the mesons the pion π^+ ($u\bar{d}$).

Similar to quarks, the leptons are also structured into three generations. These generations consist of one of the charged particles electron e^-, muon μ^-, and tau τ^- and their corresponding neutrinos ν_e, ν_μ, ν_τ. The charged particles all carry the electric charge $Q = -e$ and only differ in mass. An overview on leptons including their charge mass and lepton number is provided in table 1.3. So-called Lepton numbers have to be conserved during an interaction. For example, for the electron e^- and electron neutrino ν_e the Lepton number is $L = 1, L_e = 1, L_\mu = 0, L_\tau = 0$. For the antiparticles e^+ and $\bar{\nu}_e$:

Table 1.3: Leptons in the SM [7]. Note: neutrinos are massless in the SM. Lepton numbers are negative for antileptons.

Generation	1st	2nd	3rd
Symbol	e^-	μ^-	τ^-
Charge [e]	-1	-1	-1
Mass	511 keV	106 MeV	1.78 GeV
Symbol	ν_e	ν_μ	ν_τ
Charge [e]	0	0	0
Mass	< 2.2 eV	< 0.17 MeV	< 15.5 MeV
L	1	1	1
L_e	1	0	0
L_μ	0	1	0
L_τ	0	0	1

$L = -1, L_e = -1, L_\mu = 0, L_\tau = 0$ [30]. This is concluded with the experiment that proved that $\nu_e \neq \nu_\mu$ [16]. Lederman, Schwartz, and Steinberger accelerated 15 GeV protons on a Beryllium target, which produced pions and kaons (mesons) decaying into muons and (muon-)neutrinos (or their respective antiparticles). The detector is shielded from the muons and hadrons so that only neutrinos interact with the detector where they would produce muons or (if $\nu_e = \nu_\mu$) muons and electrons. There was evidence for 51 muons from $\bar{\nu}_\mu n \to \mu^+ p$ or $\nu_\mu n \to \mu^- p$, but none for an electron or positron. Thus, ν_e and ν_μ are not identical and the Lepton flavor numbers have been introduced. An overview of Lepton numbers is also given in table 1.3.

There are still many open questions regarding the neutrino. The general Lepton number L has been introduced after similar experiments (comparison of cross-sections) concluded that $\nu_e \neq \bar{\nu}_e$. However, the results can also be explained by the helicity, which is the projection of spin onto the momentum, which always have been observed to be -1 for ν and +1 for $\bar{\nu}$. In order to resolve this, the mass of the neutrinos is highly relevant. In the scope of SM, neutrinos are massless.Especially the observation of neutrino oscillation has indicated otherwise.
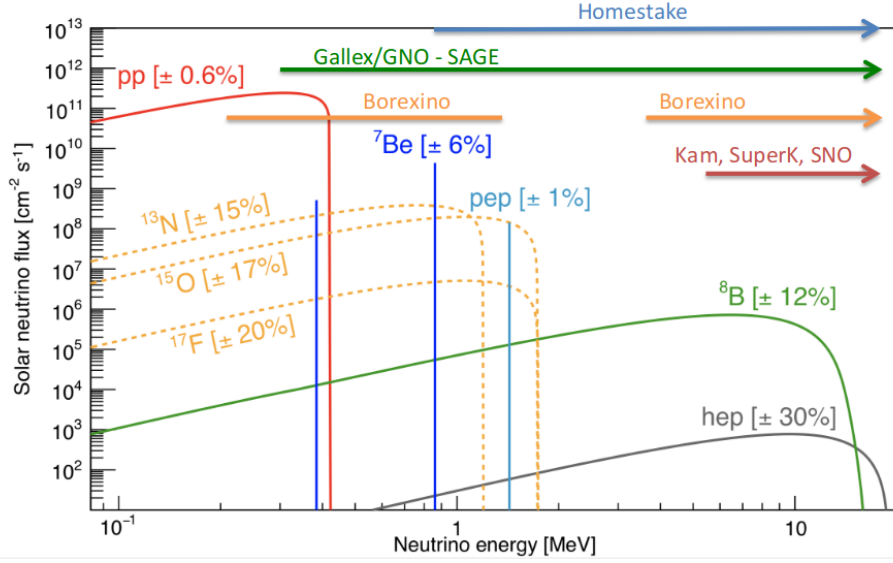
Figure 1.2: The solar neutrino energy spectrum [31]. The energy ranges of famous solar neutrino experiments are indicated at the top of the graph.

1.2 Neutrino Oscillation

Solar Neutrinos

The dominating nuclear fusion process in the sun, the pp-chain, releases neutrinos at various stages throughout the process of fusing protons into helium nuclei. The majority of neutrinos carries an energy $E_\nu < 0.5$ MeV and is difficult to detect. The much rarer decay of boron-8, produced in the fusion of two helium nuclei, releases neutrinos with energies up to 15 MeV [33]. The solar neutrino energy spectrum is shown in figure 1.2. These neutrinos were measured in the famous Homestake experiment [8]. The expectation of 1.7 interactions with solar neutrinos per day was not fulfilled, only 0.48 ± 0.04 interactions per day have been measured. This deficit became known as the solar neutrino problem. The SNO and the Super-Kamiokande experiments then provided evidence that this can be explained by neutrino oscillations [33]: The neutrino flux is consistent when regarding the sum of all three flavours; the solar neutrino deficit is apparent when observing only electron neutrinos.

General Explanation

Neutrino Oscillation is the process of one neutrino flavour transitioning into another neutrino flavour,

$$\nu_\alpha \longleftrightarrow \nu_\beta \quad \text{with} \quad \alpha, \beta = e, \mu, \tau \,. \tag{1.4}$$

In order for this to be possible, the Lepton numbers of neutrino flavours must not strictly conserved and there must be differences of masses between the flavours [30]. The latter

also indicates that not all neutrinos can be massless. Both of these requirements leave the theory of SM. However, they do not violate the fundamental physical principles of the SM [30].

Neutrinos always interact in their flavour eigenstates. There is no mathematical requirement for them to be identical with the mass eigenstates. The flavour eigenstates are rather linear combinations of the mass eigenstates. Because of the different masses, the mass eigenstates propagate in time with different phases. As a result, a pure flavour eigenstate propagating in time will result in a time-dependent mixing of flavour eigenstates. Therefore, a neutrino $|\nu_\alpha\rangle$ can be detected as $|\nu_\beta\rangle$, $\alpha \neq \beta$ at a later time. Consider the following notation

$$|\nu_\alpha\rangle \text{ orthonormal flavour eigenstates} \qquad \alpha = e, \mu, \tau \qquad (1.5)$$

$$|\nu_i\rangle \text{ orthonormal mass eigenstates} \qquad i = 1, 2, 3. \qquad (1.6)$$

The eigenstates correspond to each other via a unitary transformation matrix U with entries $U_{\alpha i}$

$$|\nu_\alpha\rangle = \sum_i U_{\alpha i} |\nu_i\rangle, \qquad |\nu_i\rangle = \sum_\alpha U_{\alpha i}^* |\nu_\alpha\rangle \qquad (1.7)$$

with U^* being the conjugate transpose of U. The mass eigenstates have time t dependency

$$|\nu_i(t)\rangle = e^{-iE_i t} |\nu_i\rangle \qquad (1.8)$$

with the total neutrino energy E_i and imaginary number i in the exponent.

$$E_i = \sqrt{p^2 + m_i^2} \approx p + \frac{m_i^2}{2p} \approx E + \frac{m_i^2}{2E}, \qquad (1.9)$$

since $p \gg m_i$, $E \approx p$, with kinetic energy E, momentum p, and mass eigenvalues m_i of the mass eigenstates. A state $|\nu_\alpha\rangle = \sum_i U_{\alpha i} |\nu_i\rangle$ at time $t = 0$ therefore propagates with

$$|\nu(t)\rangle = \sum_i U_{\alpha i} e^{-iE_i t} |\nu_i\rangle = \sum_{i,\beta} U_{\alpha i} U_{\beta i}^* e^{-iE_i t} |\nu_\beta\rangle. \qquad (1.10)$$

The transition amplitude for flavour transition $\nu_\alpha \to \nu_\beta$ is

$$A(\alpha \to \beta; t) = \langle \nu_\beta | \nu(t) \rangle = \sum_i U_{\alpha i} U_{\beta i}^* e^{-iE_i t} \qquad (1.11)$$

$$= \sum_i U_{\alpha i} U_{\beta i}^* \exp\left(-i \frac{m_i^2}{2} \frac{L}{E}\right) = A(\alpha \to \beta; L) \qquad (1.12)$$

with the propagation length $L = ct$, $c = 1$. This leads to the transition probability

$$P(\alpha \to \beta; t) = |A(\alpha \to \beta; t)|^2 = \sum_i |U_{\alpha i} U_{\beta i}^*|^2 + 2\mathrm{Re} \sum_{j>i} U_{\alpha i} U_{\alpha j}^* U_{\beta i}^* U_{\beta j} e^{-i\Delta_{ij}(t)}. \qquad (1.13)$$
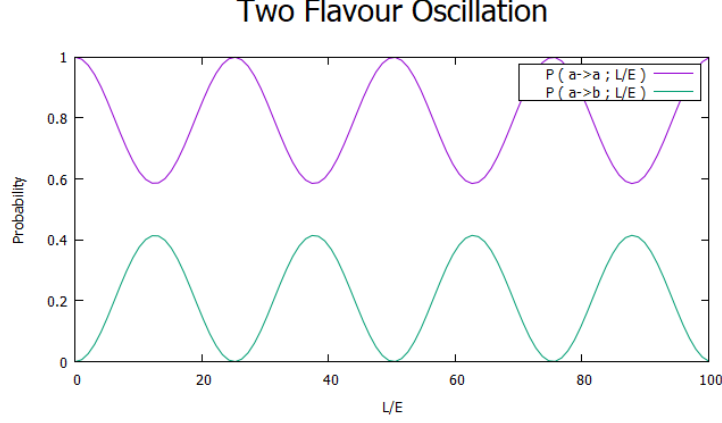
Figure 1.3: A representation of two flavour oscillation. The parameters were chosen arbitrarily.

The first term represents the mean transition probability. The second term represents the time dependent neutrino oscillations and contains the phase difference

$$\Delta_{ij} = (E_i - E_j)t = \frac{\Delta m_{ij}^2}{2} \frac{L}{E}, \quad \text{with} \quad \Delta m_{ij}^2 = m_i^2 - m_j^2. \tag{1.14}$$

Two Flavour-Oscillation

The simplest case is a mixing of only two flavours a and b, for example $\nu_e \longleftrightarrow \nu_\mu$. The transformation is

$$\begin{pmatrix} \nu_a \\ \nu_b \end{pmatrix} = \begin{pmatrix} \cos\theta & \sin\theta \\ -\sin\theta & \cos\theta \end{pmatrix} \begin{pmatrix} \nu_1 \\ \nu_2 \end{pmatrix} \tag{1.15}$$

with mixing angle $0 \leq \theta \leq \frac{\pi}{2}$ and mass difference $\Delta m^2 = m_2^2 - m_1^2$. The transition probabilities are now

$$P(\nu_a \to \nu_b) = \sin^2 2\theta \cdot \sin^2 \frac{\Delta}{2} \tag{1.16}$$

$$P(\nu_a \to \nu_a) = 1 - P(\nu_a \to \nu_b) \tag{1.17}$$

with

$$\Delta = \frac{\Delta m^2}{2} \frac{L}{E} = 2\pi \frac{L}{L_0}. \tag{1.18}$$

L_0 is called oscillation length.

This indicates that for oscillation to happen $\theta \neq 0$ and $\Delta m^2 \neq 0$ are required. The mixing angle controls the amplitude of transition, the mass difference controls the frequency. The propagation of 2 flavour oscillation is shown in figure 1.3.
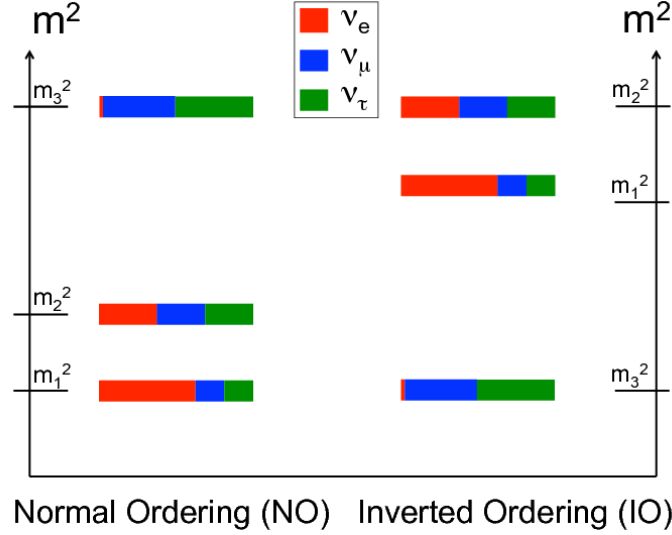
10

Figure 1.4: The mass ordering [4]. Note that the graph is not scaled since $\Delta m^2_{31} \gg \Delta m^2_{21}$. The colors represent the proportion of flavour eigenstates in the mass eigenstate.

Three Flavour Mixing

The realistic case with 3 flavours is much more complicated. There are three mixing angles θ_{ij}, a CP-violating phase Δ and two independent mass differences Δm^2_{31} and Δm^2_{21}. The sign of Δm^2_{31} could not yet have been resolved. This leaves us with the important question of the mass ordering often referred to as mass hierarchy. The two possibilities are

$$\text{Normal Ordering (NO)} \qquad m_1 < m_2 < m_3 \qquad \text{and} \qquad (1.19)$$

$$\text{Inverted Ordering (IO)} \qquad m_3 < m_1 < m_2 \,. \qquad (1.20)$$

A representation of the mass ordering is given in figure 1.4. An overview on oscillation parameters is given in table 1.4. At the L/E-value relevant for JUNO, the survival probability of an anti-electron-neutrino is approximately

$$P_{\bar{\nu}_e \bar{\nu}_e} = 1 - P_{21} - P_{31} - P_{32} \quad \text{with} \qquad (1.21)$$

$$P_{21} = \cos^4 \theta_{13} \sin^2 2\theta_{12} \sin^2 \Delta_{21} \qquad (1.22)$$

$$P_{31} = \cos^2 \theta_{12} \sin^2 2\theta_{13} \sin^2 \Delta_{31} \qquad (1.23)$$

$$P_{32} = \sin^2 \theta_{12} \sin^2 2\theta_{13} \sin^2 \Delta_{32} \qquad (1.24)$$

$$\Delta_{ij} = \frac{\Delta m^2_{ij} L}{4E} \,. \qquad (1.25)$$

P_{21} dominates the oscillation [20]. The subdominant oscillations of P_{31} and P_{32} are dependant on Δm^2_{32} and Δm^2_{31}. Therefore, there are two possible cases, dependant on the mass ordering, shown in figure 1.5. By determining the subdominant oscillation pattern, JUNO will identify the mass ordering. More information on how JUNO aims to achieve
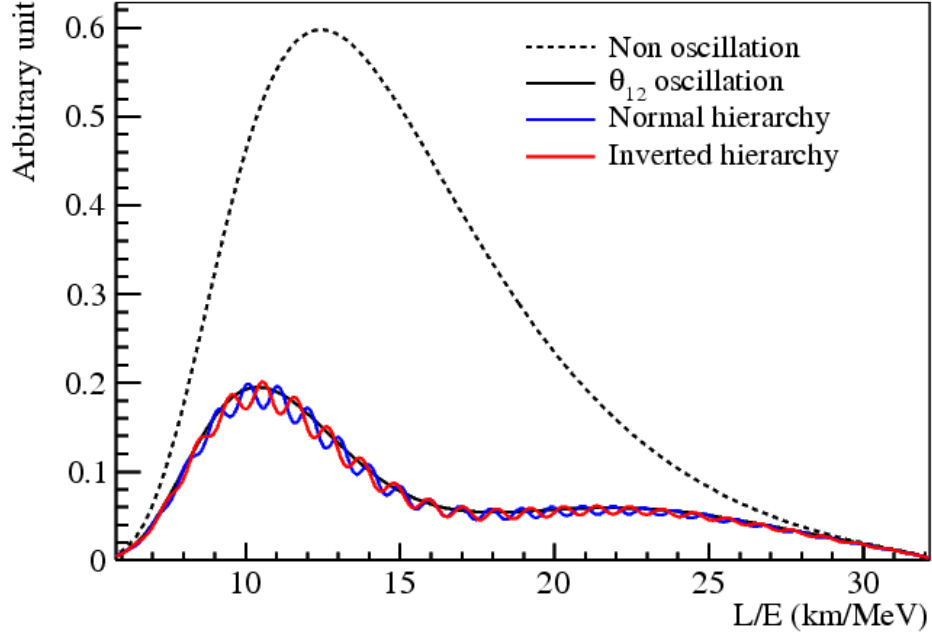
Figure 1.5: Reactor neutrino spectrum at JUNO [20].

Table 1.4: Neutrino oscillation parameters from 2013 [1]

MO	Parameter		Best Fit	1σ Range
Both	Δm_{21}^2	$[10^{-5}\text{eV}^2]$	7.54	7.32-7.80
	$\sin^2\theta_{12}$	$[10^{-2}]$	3.08	2.91-3.25
NO	Δm_{31}^2	$[10^{-3}\text{eV}^2]$	2.47	2.41-2.53
	$\sin^2\theta_{13}$	$[10^{-1}]$	2.34	2.15-2.54
	$\sin^2\theta_{23}$	$[10^{-1}]$	4.37	4.14-4.70
	Δ	$[180°]$	1.39	1.22-1.77
IO	Δm_{31}^2	$[-10^{-3}\text{eV}^2]$	2.42	2.36-2.48
	$\sin^2\theta_{13}$	$[10^{-1}]$	2.40	2.18-2.59
	$\sin^2\theta_{23}$	$[10^{-1}]$	4.55	4.24-4.94
	Δ	$[180°]$	1.31	0.98-1.60

that is presented in chapter 2.

2 JUNO

In this chapter, the goals and basic setup of JUNO is presented in section 2.1, followed by further explanations of attributes relevant for this thesis. Section 2.2 discusses the function of the liquid scintillator, section 2.3 explains how the reactor neutrinos will be detected, and section 2.4 outlines the function principle and attributes of the PMTs used in JUNO.

Figure 2.1: The location of JUNO and the two power plants that serve as neutrino source [13].

2.1 Goals and Setup

JUNOs primary goal is to determine the mass ordering by measuring Δm_{13}^2. Its location is shown in figure 2.1 and is crucial in order to maximize the sensitivity of the reactor neutrino flux to the mass ordering. As discussed in section 1.2, the neutrino oscillation is dependant on L/E with the propagation length L and the neutrino energy E. As shown in figure 1.5, this is the case at $L/E \approx 10.5 \, \mathrm{km/MeV}$. Therefore, regarding the reactor neutrino energy spectrum, which is shown in figure 2.2, a distance of $53 \, \mathrm{km}$ to nuclear powerplants in Yangjiang and Taishan has been chosen. The distances to the reactors may not differ more than $500 \, \mathrm{m}$, otherwise, the oscillation structure may be cancelled
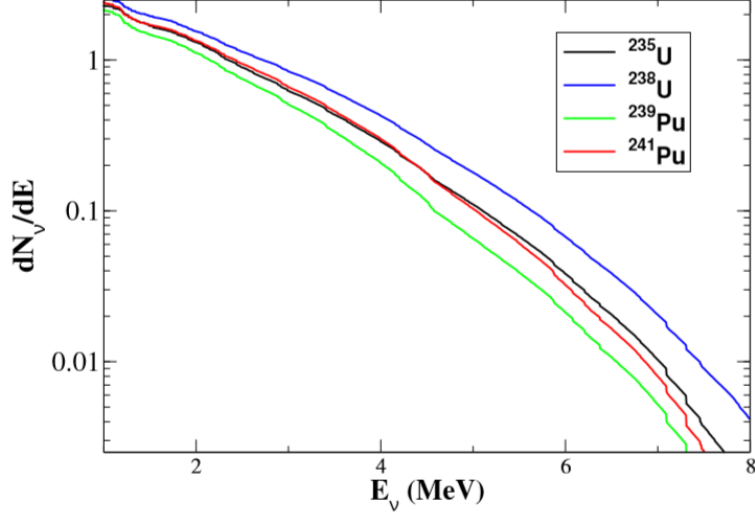
Figure 2.2: Neutrino flux from different possible fission processes in nuclear power plants [3].

Table 2.1: Oscillation Parameter Measurements at JUNO [20].

Parameter	Current Precision	Precision with JUNO
Δm_{12}^2	3%	0.6%
Δm_{23}^2	5%	0.6%
$\sin^2 \theta_{12}$	6%	0.7%

out [35]. Now, in order to reconstruct the oscillation pattern, precise measurement of the particle energy is needed. JUNO aims for an energy resolution of $3\%/\sqrt{E[\text{MeV}]}$ which has never been reached before in a large vessel LS experiment [36]. JUNO will measure other oscillation parameters with with new precision as well, as shown in table 2.1. To determine the mass ordering in the range of $3-4\sigma$ confidence, JUNO must collect data for 6 years, since 83 $\bar{\nu}_e$-events per day are expected [25]. A very important task is the elimination of background. At an expected rate of $\sim 3.5\,\text{Hz}$, cosmic and especially atmospheric muons will disturb the measurements, although large efforts are being made already to shield and reconstruct muon events.

The Central Detector (CD) of JUNO will hold 20 kton of Liquid Scintillator (LS) inside an acrylic sphere with a diameter of 35.4 m supported by stainless steel [14]. Current designs plan 17,739 20" Photomultiplier Tubes (PMTs) facing inward for event reconstruction and energy measurement. Gaps between PMTs will be filled with 36,000 3" PMTs to increase optical coverage of the sphere to ~77%. To veto muon events, the CD is placed within a pure water tank equipped with ~2000 20" PMTs for shielding and muon reconstruction via Cherenkov radiation, and muon trackers are placed on top of the CD. The entire detector is located underground with a total overburden of roughly 700 m to shield muons and other cosmic particles. A scheme of the CD is given in figure 2.3. Besides the precise measurement of oscillation parameters with reactor neutrinos, JUNO is also sensitive
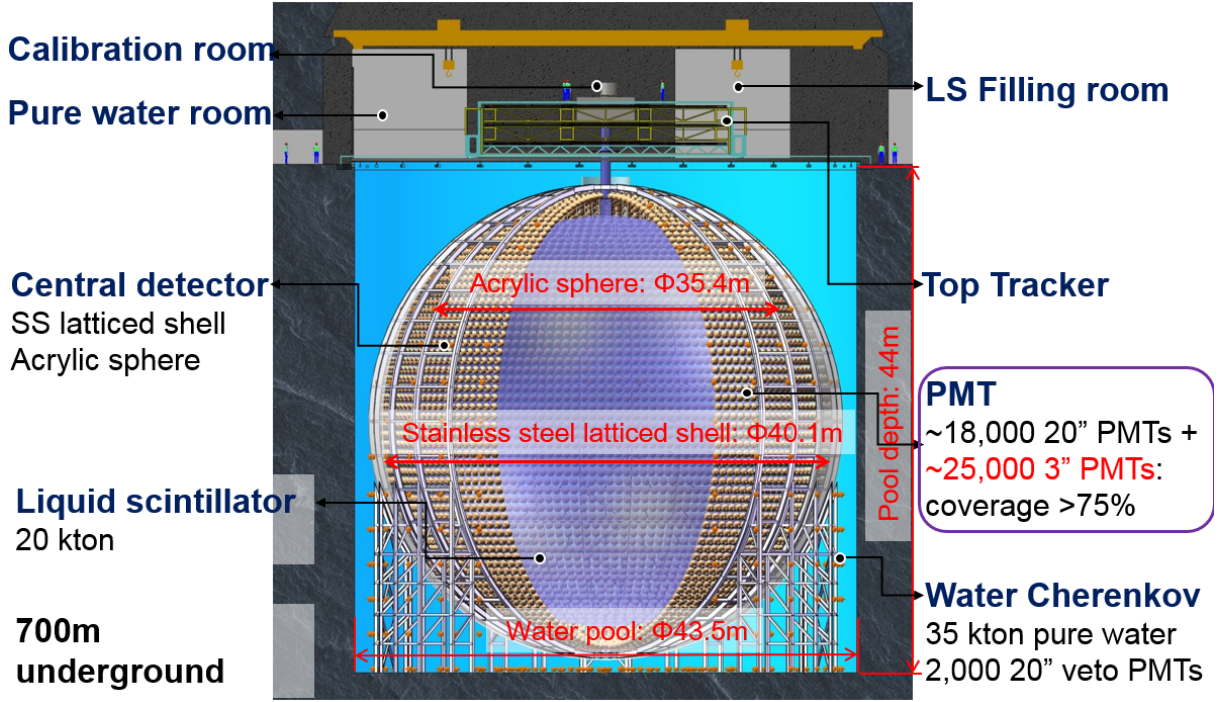
Figure 2.3: The setup of JUNO [21].

to geo-, supernova-, DSNB and atmospheric neutrinos. JUNO's size, leading to a high number of events, and JUNO's energy precision will improve the understanding of these neutrino sources.

2.2 Liquid Scintillator

JUNO is a Liquid Scintillator (LS) detector. Scintillators are materials that yield ultraviolet or visible light upon deexcitation [34]. This process is called Luminescence and, dependent on the lifespan τ of the excited state, is separated into fluorescence ($\tau \approx 10^{-9} - 10^{-8}$ s) and phosphorescence ($\tau \geq 10^{-6}$ s). In JUNO, the organic LS has several components in order to balance light yield and transparency for a maximum of photons reaching the PMTs. The basic liquid solvent is linear alkyl benzene (LAB). Its chemical formula is $C_6H_5C_nH_{2n+1}$, where C_6H_5 forms a benzene ring and n ranges from 10 to 16 [25]. LAB is excited by ionizing particles and passes this to the fluor PPO ($C_{15}H_{11}NO$) which then emits light in the ultraviolet (UV) spectrum. This wavelength is further increased by excitation and deexcitation of bis-MSB ($C_{24}H_{22}$) [25] to a wavelength of $\approx 420\,\mathrm{nm}$, at which JUNO aims for an attenuation length of $20\,\mathrm{m}$ [14] and the PMTs are most sensitive to. In order to achieve its requirements of >1,100 detected photons per MeV, tests for the concentration of PPO and bis-MSB have been concluded and the current design intends concentrations of 3g/l PPO and 15mg/l bis-MSB [5][14]. The LS is excited by charged particles that are passing through and interact with the electrons in the LS. The transmit-

ted energy excites or ionizes the molecules. In the range of $0.1 < \beta\gamma < 1000$, where β is the particle speed in terms of speed of light in vacuum $\beta = v/c$ and γ the Lorentz-factor, the Bethe Formula provides a good approximation of the differential energy deposit

$$-\frac{\mathrm{d}E}{\mathrm{d}x} = \frac{4\pi n z^2}{m_e c^2 \beta^2} \left(\frac{e^2}{4\pi\epsilon_0} \right)^2 \left[\ln \frac{2m_e c^2 \beta^2}{I \cdot (1 - \beta^2)} - \beta^2 \right] , \tag{2.1}$$

where ϵ_0 is the vacuum permittivity, e is the elementary electric charge, z is the charge of the particle in e, m_e the mass of the electron, n the electron density, and I the mean excitation energy for the target atoms [25]. Outside of this range, corrections have to be applied, for example bremsstrahlung for fast electrons [10]. About 3% of the deposited energy is re-emitted as a photon [6]. However, The light yield is not linear to the deposited energy. It is commonly approximated by Birks' Formula

$$\frac{\mathrm{d}\mathcal{L}}{\mathrm{d}x} = \mathcal{L}_0 \cdot \frac{\frac{\mathrm{d}E}{\mathrm{d}x}}{1 + k_B \frac{\mathrm{d}E}{\mathrm{d}x}} , \tag{2.2}$$

where $\mathcal{L}_0$ is typically one photon per 100 eV and k_B is Birks' constant that has to be measured in the LS [25]. Considering a linear proportionality of light yield and deposited energy, one can roughly assume a light yield of 10,000 photons per MeV. The deexcitation rate of the electron states is proportional to their population. Therefore, considering a negligible risetime, the temporal distribution of decay of a certain state can be described by an exponential decay function. The probability density function (pdf) of the overall temporal distribution of emitted photons with excitation at $t = 0$ is described by

$$\Phi_{Em} = \sum_i \frac{w_i}{\tau_i} e^{\frac{t}{\tau_i}} , \qquad t > 0, \sum_i w_i = 1 \tag{2.3}$$

where τ_i is the mean lifetime of the excited state i and w_i its relative occurrence.

2.3 Neutrino Detection

Neutrinos are neutral particles and do not deposit their energy according to the Bethe Formula. Neutrinos only interact via the weak force, often denoted as the charged current (CC), which is interaction via the $W^{+/-}$ bosons, and the neutral current (NC) via the Z boson. There are several possibilities of the $\bar{\nu}_e$ to interact with the LS with detectable products. One possibility is the elastic scattering on an electron

$$\bar{\nu}_e + e^- \longrightarrow \bar{\nu}_e + e^- \tag{2.4}$$

or a proton

$$\bar{\nu}_e + p \longrightarrow \bar{\nu}_e + p . \tag{2.5}$$

The neutrino transfers kinetic energy to a charged particle which in turn deposits it in the LS. However, even a fixed neutrino energy E_ν results in a continuous spectrum of the kinetic energy of the charged particle. Due to the higher mass of the proton, the signal from scattering on protons is much smaller than that of scattering on electrons. Elastic and inelastic interaction with nuclei is also possible and can yield characteristic signals when a positron and an unstable nucleus are the products [25]. However, most important for the identification of $\bar{\nu}_e$ is the inverse β-decay (IBD)

$$\bar{\nu}_e + p \longrightarrow e^+ + n\,. \tag{2.6}$$

Within nanoseconds, the resulting positron annihilates with an electron and releases two characteristic γs with energies of $511\,\mathrm{keV}$. The neutron will be captured mainly by hydrogen which emits a 2.2 MeV γ with an average capture time of $\sim 200\mu s$ [22]. The produced photons with high energy then further interact with the LS, mainly via Compton-scattering where kinetic energy is transferred onto charged particles. As discussed, moving charged particle deposit their energy as described by the Bethe-Formula and emit detectable scintillation light. This characteristic delayed signal of the e^+/e^--annihilation and the neutron capture make it possible to suppress background and identify the $\bar{\nu}_e$.

However, this signal can be mimicked by some background sources. Especially cosmic muons can form isotopes that decay and mimic IBD signals. The expected muon rate is $\sim 3.5\,\mathrm{Hz}$. Since it is impossible to shield this experiment from neutrinos, neutrinos not originating from Yangjiang and Taishan nuclear powerplants, for example the daya bay reactor, will also produce background signals. At last, radioactive purity of the LS and the components of the detector as well as identification of radioactive decay of the used materials are of importance. Geoneutrinos and radioactive decay in the detector material will account for ~ 1.55 events per day [23].

2.4 PMTs

The scintillation light has to be captured and registered by Photomultiplier Tubes (PMTs). Current designs intent a total of 17,739 20" PMTs facing inwards the CD. PMTs convert photons into electric signals. When entering the glass that holds the vacuum of a PMT, a photon arrives at the photocathode and with a probability called Quantum Efficiency (QE), an electron is set free due to the photoelectric effect. This photoelectron (PE) is accelerated by an electric field onto a dynode. Since the electron gained energy during acceleration, it is now able to release multiple electrons from the dynode. These are accelerated onto the next dynode and the technique is repeated until the electrons are collected by the anode. The total gain of $10^3 - 10^9$ electrons is sufficient to produce a
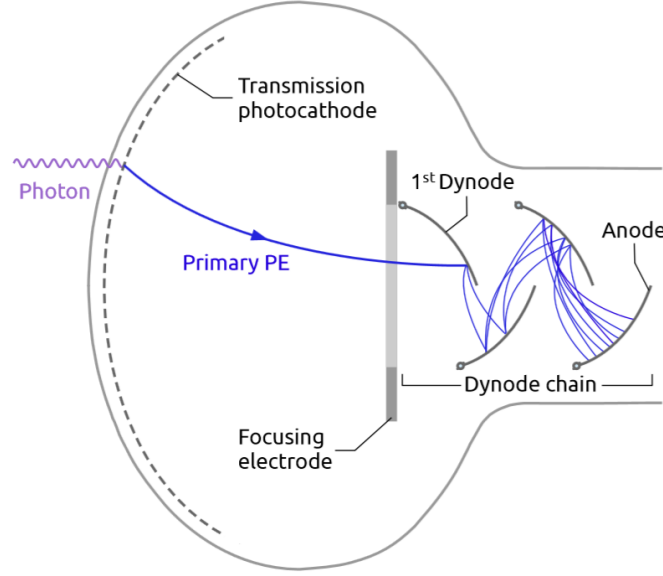
Figure 2.4: Scheme of a Dynode PMT [25].

measurable current. In order to continuously accelerate the electrons, the dynodes have to be connected with increasing voltage [12]. A schematic PMT is shown in figure 2.4. The inward facing 20" PMTs will be 4,998 dynode PMTs by manufacturer Hamamatsu, the other 12,741 will be Microchannel-plate (MCP) PMTs by manufacturer Northern Night Vision Technology (NNVT).

In MCP-PMTs, a plate with channels with the size of a few μm is used. An electric field outside of the plate accelerates the electrons through these channels. The channel walls are often coated with a semiconductor [11]. An electron is then multiplied when it hits the wall of the channel. In order to improve the detection efficiency, the MCP surface and channels are coated with a thin film of Al_2O_3 or MgO [24]. This increases the rate of secondary electrons when a PE hits the surface of the PMT instead of a channel. The secondary electron will then enter the channel and produce the signal. A scheme of a MCP is shown in figure 2.5, while the MCP-PMTs for JUNO is depicted in figure 2.6.

2.4.1 Attributes

Photon Detection Efficiency (PDE)

The PDE is the QE multiplied by the probability that the PE is directed onto the first dynode, the PE collection efficiency (CE)

$$PDE = QE \cdot CE. \tag{2.7}$$

18
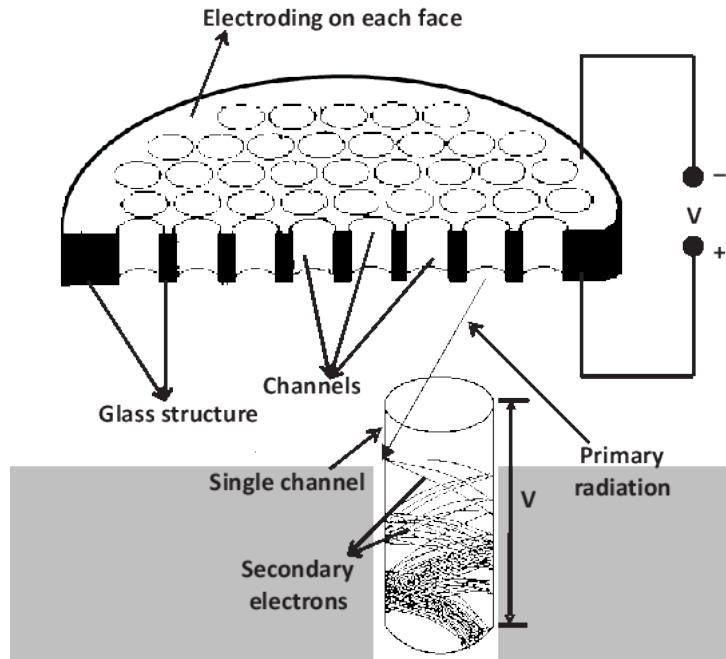
Figure 2.5: Scheme of a MCP [11]. To assure that a passing electron hits the channel wall, the channels are usually inclined, or two MCPs with opposite inclined channels used.
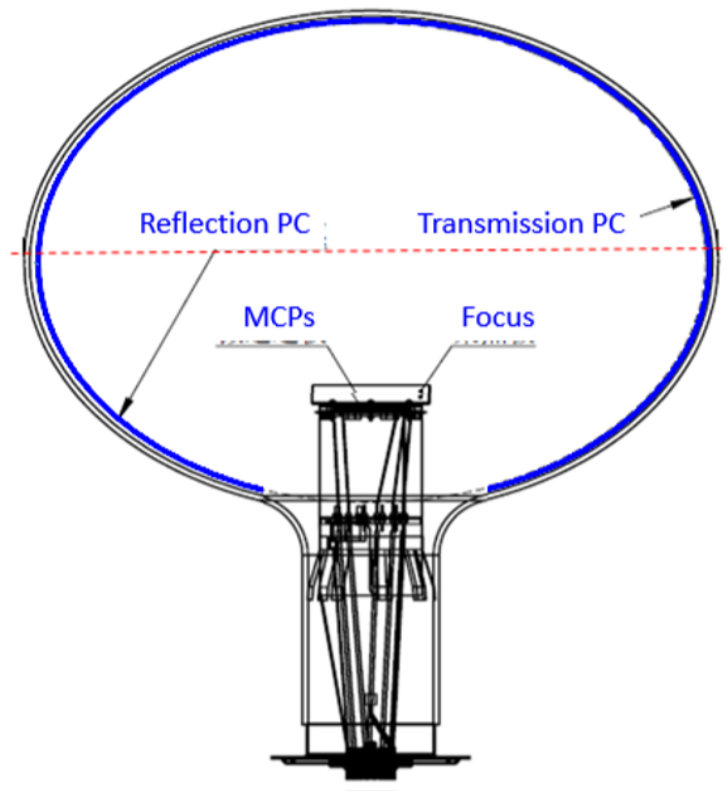
Figure 2.6: The MCP-PMT developed for JUNO [28]. Both transmissive and reflective photo cathodes are used to maximize the QE.

The PDE depends on the wavelength of the photons and to reach the expected 1,100 PE per MeV, JUNO's PMTs aim for a peak photon detection efficiency (PDE) of >30 % at 420 nm [14]. Current tests determined a mean PDE of 28.1% for both PMT-types in the relevant photon spectrum [19].

Transit Time Spread (TTS)

The time between production of a PE and the collection of electrons at the anode is called transit time. It strongly depends on the position on the photocathode where the PE is produced and thus what path it takes before being collected at the first dynode or MCP. The Transit Time Spread (TTS) is defined as the Full-Width-Half-Maximum (FWHM) of the distribution of the transit time. The TTS has been tested to be 2.8 ns for the dynode-PMTs and 20.2 ns for the MCP-PMTs. The large TTS of the MCP-PMTs is especially bad for topological reconstruction, since the time of photon arrival together with its speed delivers crucial spatial information. However, it increases the chance of two PE at nearly the same time to be identified as such, generating two different peaks.

Pulse

The resulting cascade of electrons produce an electric signal depicted in figure 2.7. The shown measurements were produced in tests that each PMT has to pass before being admitted. These tests involve analysis of the SPE Pulse Wave. For that, a triggered light signal with an expectation of 0.1 PE per frame is directed onto the PMT. The electronic readout system has a sampling rate of 1 GS/s, which corresponds to 1 point per nanosecond.
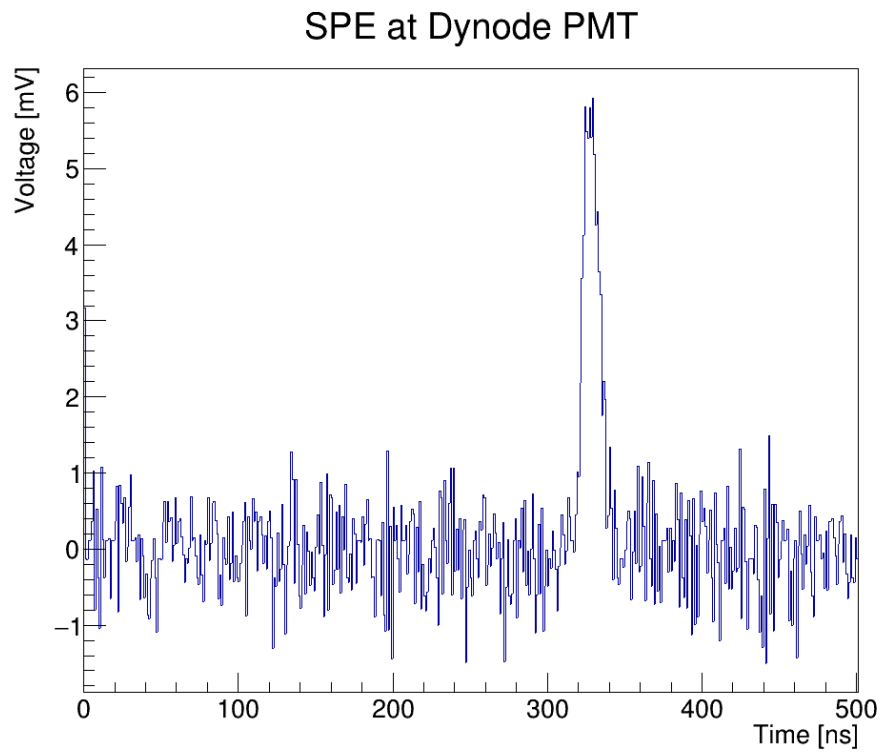
(a) SPE signal at Dynode PMT.
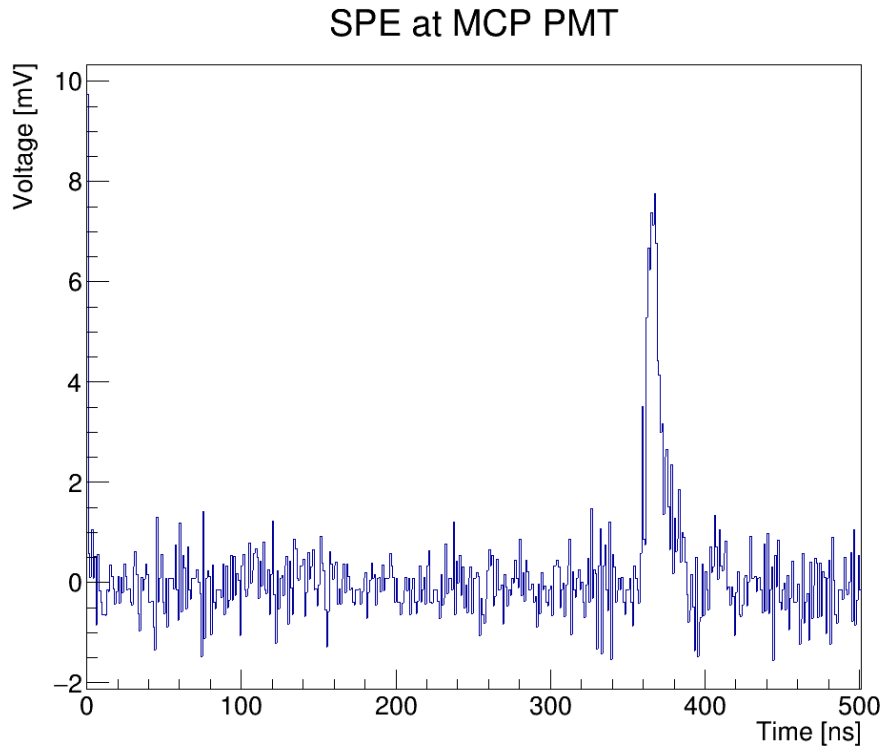
(b) SPE signal at MCP PMT.

Figure 2.7: Examples for SPE Signals for both PMT Types.
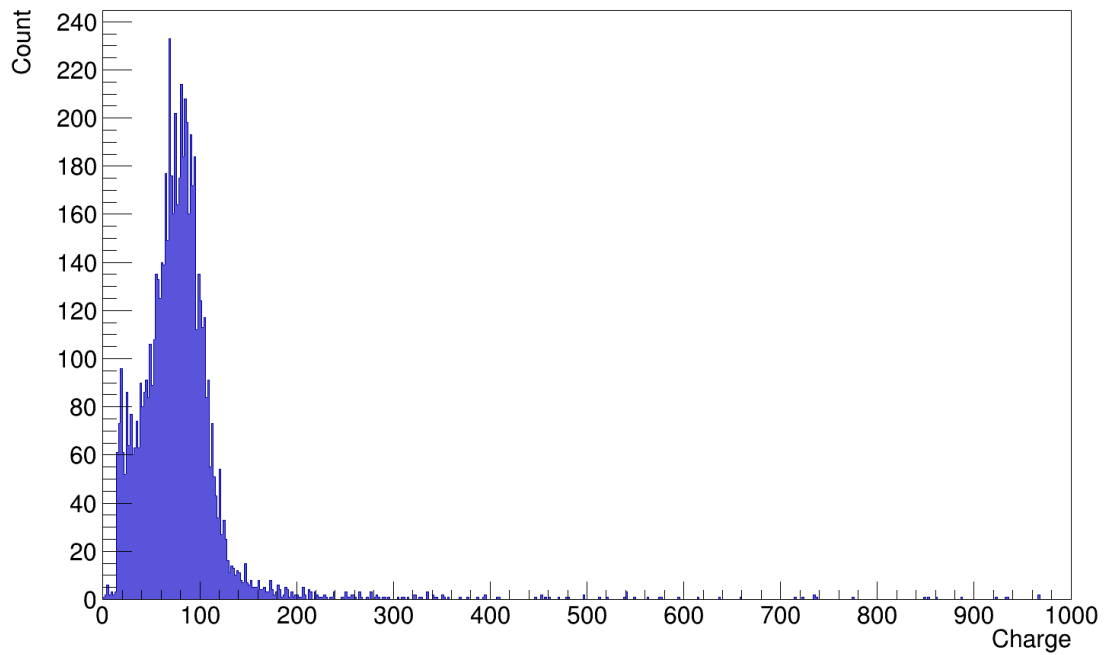
Charge Distribution

Each electrons arriving at the anode deposit a charge of e. All n_e electrons of a PE-Signal therefore deposit the accumulated Charge $Q = n_e \times e$. This is proportional to the area beneath the pulse form shown in figue 2.7. In the scope of this thesis, the term charge always refers to the area beneath the pulse wave and will never be converted to the proper units ($\sim$pC range). The charge distribution will be crucial for energy reconstruction. The measured charge distribution for SPE events for both PMTs are shown in figure 2.8

The data stems from the same measurements as the examples for the SPE pulse waves, since the SPE signal is of importance. To create these charge distributions, scripts provided by Micheala Schever have been lightly altered and used to analyze the charge of PMTs that serve as reference PMTs in the testing system and have thus been tested multiple times. The used data is for the dynode PMT with serial number EA0419 and MCP PMT PA1704-731 in mass258- mass367.

Spurious Signal Pulses

When a photon produces a PE in another way as described above or at a part of the PMT other than the photocathode, a pre-pulse or an after-pulse can occur. The PMT will measure a peak at the wrong time, because of the different transit time. To avoid these peaks with false arrival time and to avoid counting two signals from the same photon as two photons, they have to be filtered out effectively [25]. Radiation of materials used in the PMT and thermally emitted electrons can also yield signals, often referred to as dark current. Since the PE are quite slow and electrically charged, they are sensitive to earth's magnetic field. Thus, a large coil system is built around the CD.

Dynode PMT Charge Distribution

(a) Charge distribution at Dynode PMT.

MCP PMT Charge Distribution
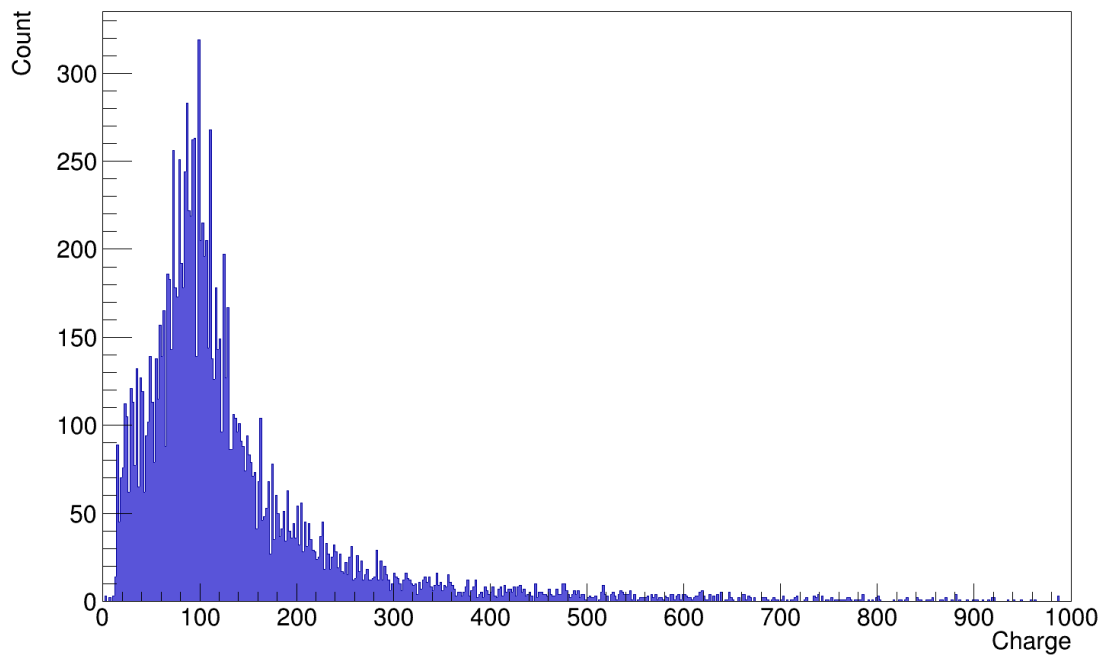
(b) Charge distribution at MCP PMT.

Figure 2.8: The SPE Charge distribution for both PMT Types. The MCP PMT has a broader spectrum, especially reaching out to very high values. At the left side of the dynode PMT spectrum one can see an additional peak, that are remnants from noise signals. The same appears for MCP PMTs, however it is not as visible in this representation.

2.5 Energy Reconstruction

As mentioned before, not all deposited energy will convert into PE or even photons. With the number of registered photons an estimation of this visible energy is possible and an estimate for the invisible energy has to be calculated according to the type of event in order to reconstruct the total event energy. In the scope of this thesis, the visible energy is the only energy estimate taken into account. With knowledge about light yield (LY) and local detection efficiency (LDE) describing the probability of an emitted photon to be detected, an estimation of energy can be given by the number of PE (N_{PE})

$$\hat{E} = \frac{N_{PE}}{\text{LDE} \times \text{LY}} \,.$$

(2.8)

Derived from poisson statistics the relative energy resolution σ_E mainly depends on N_{PE}

$$\sigma_E \approx \frac{1}{\sqrt{N_{PE}}} \,.$$

(2.9)

This indicates why the goal of $\sigma_E \approx 3\%$ at 1 MeV requires the 1,100 PE per MeV. There are two commonly used techniques to retrieve N_{PE}. First, the peaks of signals shown in figure 2.7 can be counted. This peak counting (PC) can fail when noise is wrongfully counted and when the signals of the PE overlap heavily. The latter will always cause an increasing lack of PE with increasing energy, since multi-photon hits at the PMTs will become more likely. This effect can be calibrated, but the loss of information also yields a lower resolution. The method of charge integration (CI) summarizes the area of these waveforms for every event. This sum is then divided by the mean SPE-charge of the spectra shown in 2.8. The elongated charge distribution as well as strong overlapping of two photoelectron (TPE) charge distribution of the MCP-PMTs decreases accuracy for this method.

2.5.1 Likelihood Method

The likelihood method to be tested will combine multiple information to provide an improved guess for the number of PE. At first an energy guess E_{Guess} provided by PC or CI is needed. Based on this energy guess and with knowledge of vertex position of the event, the expectation value for the number of PE at each PMT is calculated. This process is further discussed in the next chapter. The expectation value yields information on the probabilities of different number of PE at the PMT. The normalized charge spectrum for each number of PE is scaled with its probability. The height of these weighted spectrums at the measured Charge at the PMT is examined, which yields a more accurate probability for the number of PE at each PMT and a new energy guess can be reconstructed. The

mathematical details can be found in section 3.4, where the implementation in the toy simulation is explained. One can add additional information, such as the time distribution to implement the probability of overlapping PE signals.

3 Methods for Simulating Detector Signals and Reconstructing Energy

In order to estimate the influence of the charge distribution and the effectivity of the likelihood-method, a Toy-Monte-Carlo Simulation (TMC) is constructed. In Monte Carlo Simulations (MC), the physical problem is approximated by generating random numbers according to a known distribution of that number. TMCs do not aim to simulate the whole underlying physical process, but rather the most important aspects for the given problem, which eases the analysis of the results [26]. Thus, TMCs are commonly used to test hypothesises. In this TMC, an event with a given energy and position within the CD is the starting point. Then, the number of PE and the resulting signals at the PMT have to be simulated, which then will be analyzed to test the energy reconstruction methods. Although an extensive JUNO simulation based on the GEANT4 platform is available, a TMC has the aforementioned advantage of straightforward analysis but also provides full control of the simulation parameters.

The TMC is written in C++ using the ROOT framework developed by Cern. ROOT is designed to process large amounts of data and provides many functions in terms of histograms, fitting, data storage and accessibility. This chapter describes the stages of the simulation in chronological order. Section 3.1 starts with the calculation of the expected PE at every PMT, in section 3.2 the construction of the PMT signal is outlined. The methods of analyzing the signal at each PMT is explained in section 3.3, while the energy reconstruction is gcovered +. in section 3.4. Section 3.5 then outlines the output given by the simulation of an event and how it is processed and analyzed.

3.1 Hit Probability

The number of total PE is dependent on deposited energy, event position in the detector, light yield, light attenuation and PDE of the PMTs. To resolve this, results from the mentioned JUNO simulation are used. In order to simulate scintillation light and minimize other effects like Cherenkov radiation or positron/electron annihilation, an electron with a kinetic energy of 0.5 MeV with random positions throughout the LS has been simulated

one million times. The results are used to calculate the total photon emission and to generate a look-up table used to calculate the probability of a hit at a certain PMT.

3.1.1 Light Yield

In order to retrieve the light yield, the mentioned simulation has been repeated at 1 and 3 MeV. As mentioned before, the light yield is not linear to the deposited energy, however a linear light yield is assumed in the TMC. A linear fit of the simulation data has yielded the parameters

$$b = 13137 \pm 51 \quad c = -752 \pm 95 \,, \tag{3.1}$$

for the linear fit

$$\langle N_{EM} \rangle \left(E \,[\text{MeV}] \right) = b \cdot E \,[\text{MeV}] + c \,. \tag{3.2}$$

This approximation is used in the TMC to generate the expectation of N_{EM}. The total light yield is subject to statistical fluctuations. In this TMC, a gaussian distribution G with a σ according to Poisson statistics is used

$$\sigma_{EM} = \sqrt{N_{EM}} \,. \tag{3.3}$$

The total photons emitted N_{EM} is therefore calculated with

$$N_{EM}(E) = \langle N_{EM} \rangle \left(E \right) + \texttt{Rand}(G_{\sigma_{EM}}) \,, \tag{3.4}$$

where $\texttt{Rand}(f)$ returns a random number weighted with function f. The gaussian here has a mean of zero and a sigma as shown in equation (3.3).

3.1.2 Look Up Table

Everything that is described from now until section 3.4 happens inside a loop over all 17,739 PMTs. For this, a file containing the id, position, and type of PMT (dynode or MCP) is used. To retrieve an expectation $\langle n_i \rangle$ for PE at PMT i, a look-up table has been created. It describes the probability of a photon with distance d and angle θ to the PMTs surface to result in a PE. It contains all effects included in the JUNO simulation such as attenuation, scattering, solid angle and PMT QE. The QE used in the JUNO simulation is shown in figure 3.1. A 2D-Histogram has been created by looping over all PMTs for every event and storing the number of PE n_{PE} and N_{EM} in respect to d and θ. This yields the look-up table (LUT) value

$$\text{LUT}(d_0, \theta_0) = \frac{\sum_{d=d_0, \theta=\theta_0} n}{\sum_{d=d_0, \theta=\theta_0} N_{EM}} \tag{3.5}$$
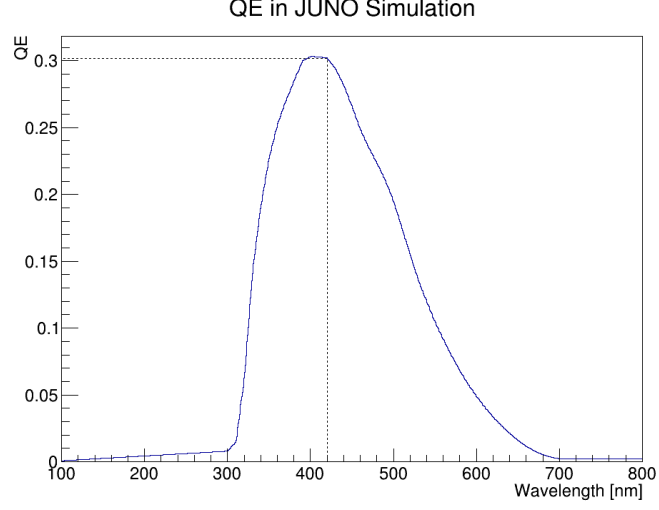
Figure 3.1: The QE used in the JUNO Simulation. At 420 nm, the QE is 30.2%.

Therefore, $\langle n_i \rangle$ is calculated via

$$\langle n_i \rangle = N_{EM} \times \mathrm{LUT}(d_i, \theta_i)\,, \tag{3.6}$$

$$d_i = |\vec{r}_i - \vec{R}|\,, \quad \theta_i = \measuredangle(\vec{r}_i, \vec{R})\,, \tag{3.7}$$

Aus Simulation mit e^- mit 0.5 MeV:

$$\mathrm{LUT}(d_0, \theta_0) = \frac{\sum_{d=d_0,\theta=\theta_0} n}{\sum_{d=d_0,\theta=\theta_0} N_{EM}} \tag{3.8}$$

where $\vec{r}_i$ is the position of PMT i and $\vec{R}$ the position of the event, both relative to the center of the CD. The resulting LUT is shown in figure 3.2.
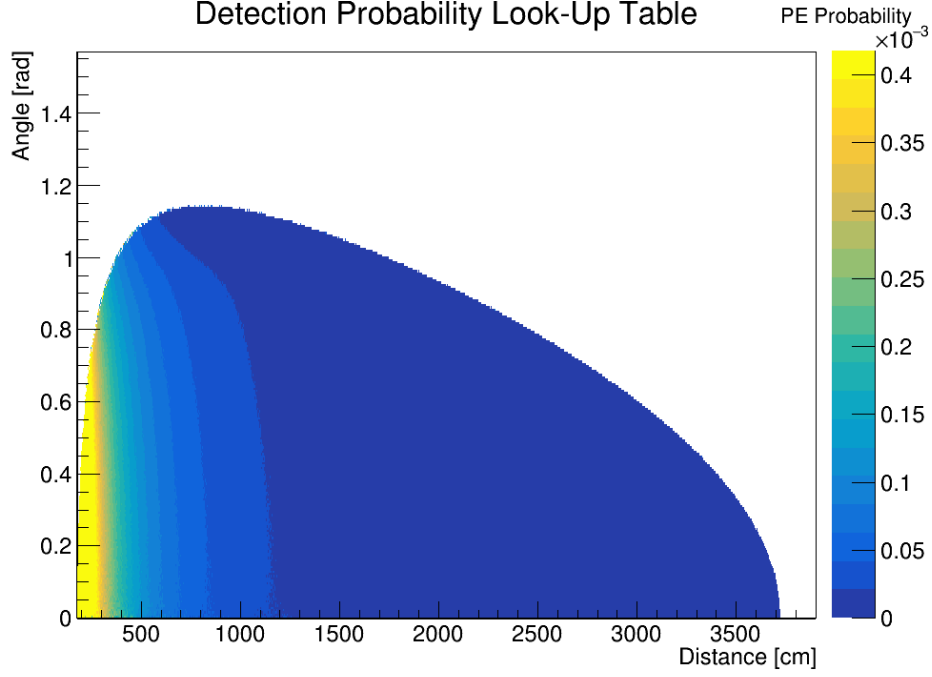
Figure 3.2: The generated Look-Up Table at $E = 0.5\,\mathrm{MeV}$. It describes the probability of an emitted photon to result in a PE at given distance and angle to the PMT.

To improve the statistics at critical places in the CD, for example the center which has a tiny volume and is the only place where $(d, \theta) = (1950\text{ cm}, 0)$, multiple simulations at center and at the edge have been repeated and appended in the manner described by equation (3.8). However, a lack of statistics and thus a lack of reliability is still present close to the edge of the CD and at $\theta < 0.04$ rad. This effect can be seen in figure 3.3. Therefore, a threshold for θ has been introduced

$$\text{if } \theta < 0.04 \Rightarrow \theta = 0.04\,, \tag{3.9}$$

and running the TMC at positions very close to the acrylic sphere yield unreliable results. Profiles of the LUT are shown in figure 3.4.
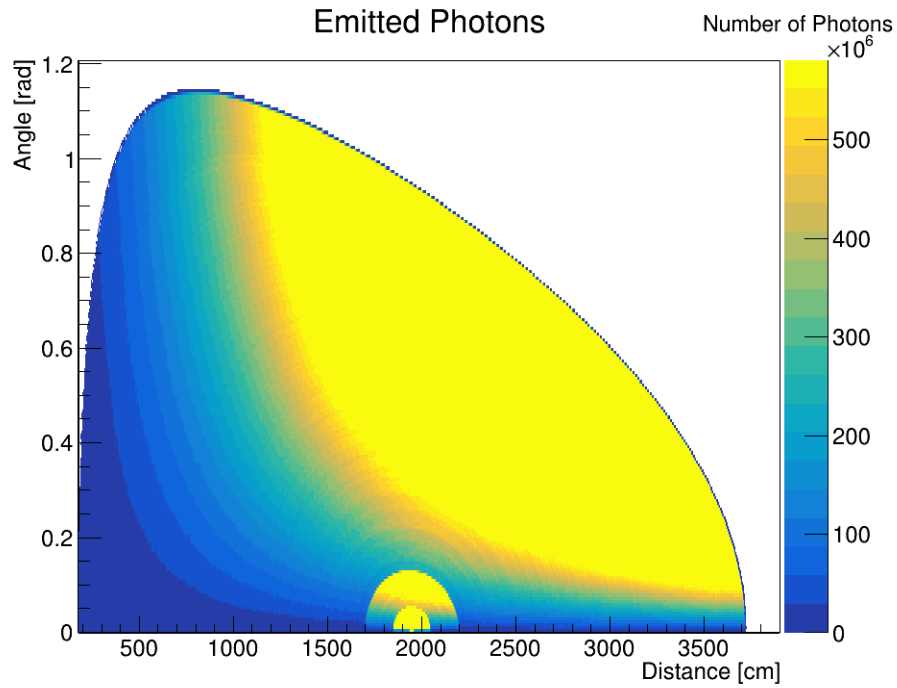
Figure 3.3: The Emitted Photons relative to Distance and Angle of the PMTs which equals the denomiator in equation 3.8 and serves as reference to the number of events. The bright areas have data of >200,000 events, while some of the extreme areas close to the edge only contain data of a few hundred events. The bright areas in the center stem from the multiple additional simulations to decrease statistical fluctuation at the center of the CD.

Influence of distance on Hit probability
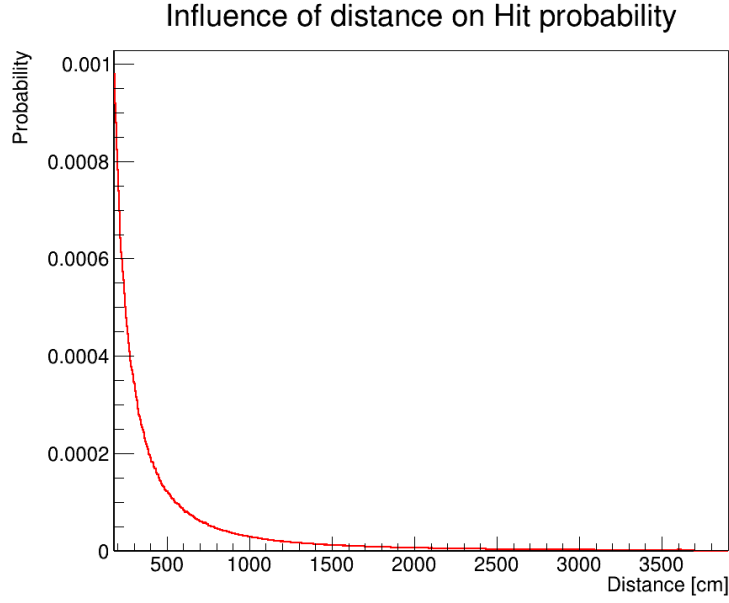
(a) The LUT Profile at $\theta = 0.12\,\mathrm{rad}$.

Influence of angle on Hit probability
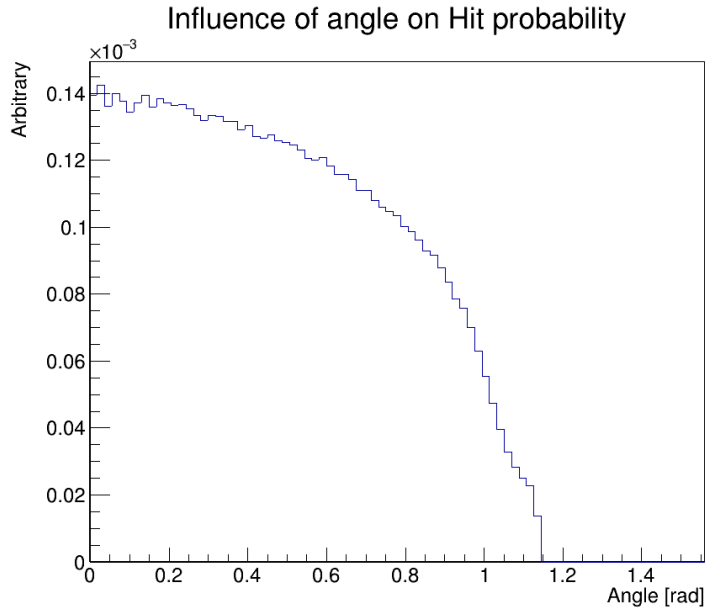
(b) The LUT Profile at $d = 800\,\mathrm{cm}$.

Figure 3.4: The Profiles of the LUT. The detection probability heavily depends on the solid angle to the PMT. Close to the PMT the solid angle is large and attenuation unlikely, however an event close to the edge yields a steep angle to many PMTs at which the solid angle shrinks. Effects of refraction at the acrylic sphere also reduce detection at the edge of the CD.

3.2 Generating Signals

At every PMT, the number of PE and the resulting signal have to be rolled. These should mimic the signals shown in section 2.4.1. For each PMT, a Histogram with 300 bins, each bin representing 1 ns, is created. For each PE, amplitude and arrival time have to be determined and the corresponding SPE wave is added to the PMT Signal. Finally, noise is added.

3.2.1 Number of PE

The number of PE produced is Poisson distributed and is therefore retrieved by generating a random number weighted with the integral Poisson distribution PI with an expectation value of $\langle n_i \rangle$, where PI has the value of the $P(n)$ between n and $n + 1$, when P is the Poisson distribution. PI is shown in figure 3.5.
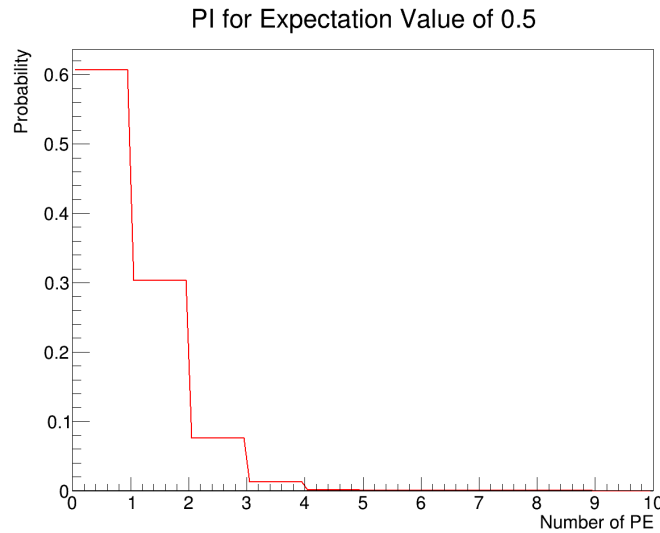
Figure 3.5: The Integral Poisson Distribution for $\langle n_i \rangle = 0.5$. The possibility that no PE is produced is $\sim 60\%$, one PE has chance of $\sim 30\%$ and the rest distributes on two or more PE.

Therefore,

$$n_i = \texttt{Rand}(PI_{\langle n_i \rangle}) . \tag{3.10}$$

n_i is then round down to become an integer and is the number of PE at PMT i.

3.2.2 Pulse Shape

Every PMT should mimic a signal similar to the signal the DAQ in the test containers produces, discussed in section 2.4.1. Therefore, a histogram with a bin width of 1 ns
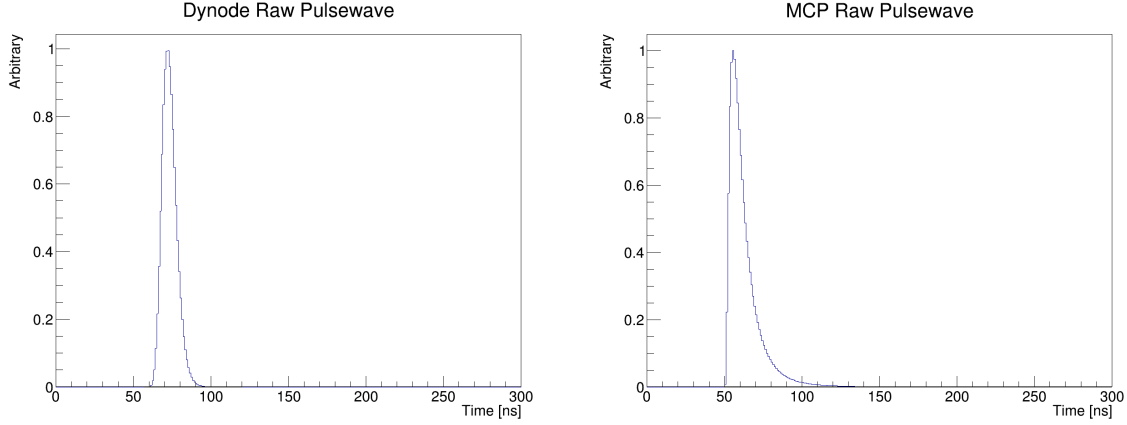
(a) Pulse form at dynode PMTs.

(b) Pulse Form at MCP PMTs

Figure 3.6: The raw log-normal pulse form. $U = 1$ and $T = 50$ have been chosen

is created and will be filled with pulse waves from every PE and with noise. The pulse shape is currently being studied, but a good approximation is given by the log-normal distribution

$$f(t) = \begin{cases} U \cdot \exp\left(-\frac{1}{2}\left(\frac{\ln\left(\frac{t-T}{\tau}\right)}{\sigma}\right)\right) & \text{if } T > t \\ 0 & \text{else} \end{cases} \tag{3.11}$$

with amplitude U, time of arrival of signal T and the function parameters τ and σ that have to be retrieved from fitting SPE waveforms. τ and σ are correlated and not yet fully understood. However, mean values will be used for each PMT type and have been kindly provided by Michaela Schever from Forschungszentrum Jülich. The used parameters are

$$\text{MCP}: \quad \tau = 5.5, \quad \sigma = 0.75 \tag{3.12}$$

$$\text{dynode}: \quad \tau = 22, \quad \sigma = 0.2\,. \tag{3.13}$$

The raw pulse shape of each PMT type is depicted in figure 3.6. The parameters left to determine are U and T.

3.2.3 Time of Arrival

For each PMT, only the relative times of arrival of PE at the same PMT are relevant. This especially means that the time of flight of the photons through the CD can be ignored completely. The time of arrival of the signal is mainly dependant on the emission time probability density function discussed in 2.2,

$$\Phi_{Em} = \sum_i \frac{w_i}{\tau_i} e^{\frac{t}{\tau_i}}\,, \qquad t > 0, \sum_i w_i = 1 \tag{3.14}$$
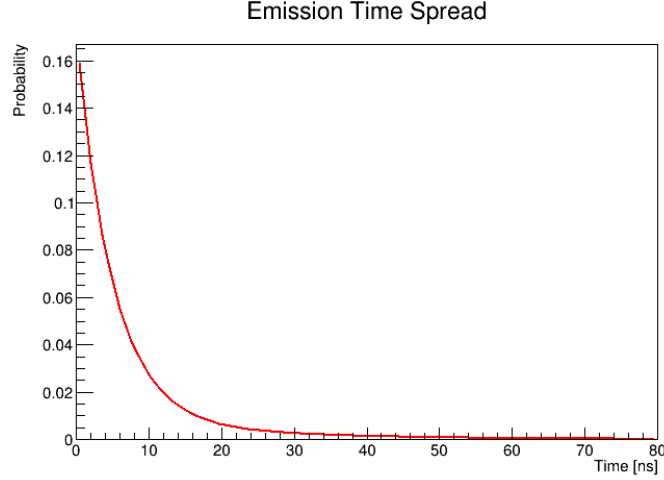
Figure 3.7: The Emission Time Spread of the LS as used in the TMC.

and the TTS of the PMT discussed in 2.4. The values for Φ_{EM} are

$$\tau_1 = 4.93\,\text{ns}\,, \qquad\qquad w_1 = 0.799\,, \qquad\qquad (3.15)$$

$$\tau_2 = 20.6\,\text{ns}\,, \qquad\qquad w_2 = 0.201\,. \qquad\qquad (3.16)$$

These values are currently used in the JUNO Simulation as well. The resulting emission time profile is shown in figure 3.7. A TTS of 2.8 ns for dynode, and 20.2 ns for MCP PMTs have been measured. In the TMC, a Gaussian distributed TTS is presumed. Therefore, with Gaussian G the time T is determined for every PE with

$$T = \texttt{Rand}(\Phi_{EM}) + \texttt{Rand}(G_{\text{FWHM=TTS}}) + 50\,\text{ns}\,. \qquad (3.17)$$

The additional 50 ns are required to keep the pulse wave within the frame as $\texttt{Rand}(G_{\text{FWHM=TTS}})$ can yield negative values.

3.2.4 Amplitude & Charge

With fixed values for the log-normal parameters τ and σ, the amplitude U and charge Q are directly correlated. Analyzing the integral of the log normal function determined that $Q \propto U$ and only a conversion factor c is needed

$$\text{MCP}: \quad Q = \int_T^\infty f(t)\mathrm{d}t = U \cdot 13.596 = U \cdot c_{\text{MCP}} \qquad (3.18)$$

$$\text{dynode}: \quad Q = \int_T^\infty f(t)\mathrm{d}t = U \cdot 11.252 = U \cdot c_{\text{Dyn}} \qquad (3.19)$$

Therefore, the amplitude U will be determined by a random weighted charge

$$U = \frac{\texttt{Rand}(Q)}{c} \, , \tag{3.20}$$

where Q is the charge distribution. In order to use the distributions shown in section 2.4 for simulation, some adjustments are made. The left side of the distribution is cut off, since the additional peaks originate from noise. Additionally, the distributions are smoothed. The resulting SPE charge distributions used in the TMC are shown in figure 3.8.

3.2.5 Noise

Some noise will be added in order to simulate the real signal. It is also important since it adds difficulties for analysis of the waveform described in the next section. In order to vary the total noise, a random number R between 1000 and 2500 is generated. Then, a signal with the height of 1.5 mV is added randomly to one of the 300 bins R-times. Examples of the final simulated SPE wave are shown in figure 3.9.
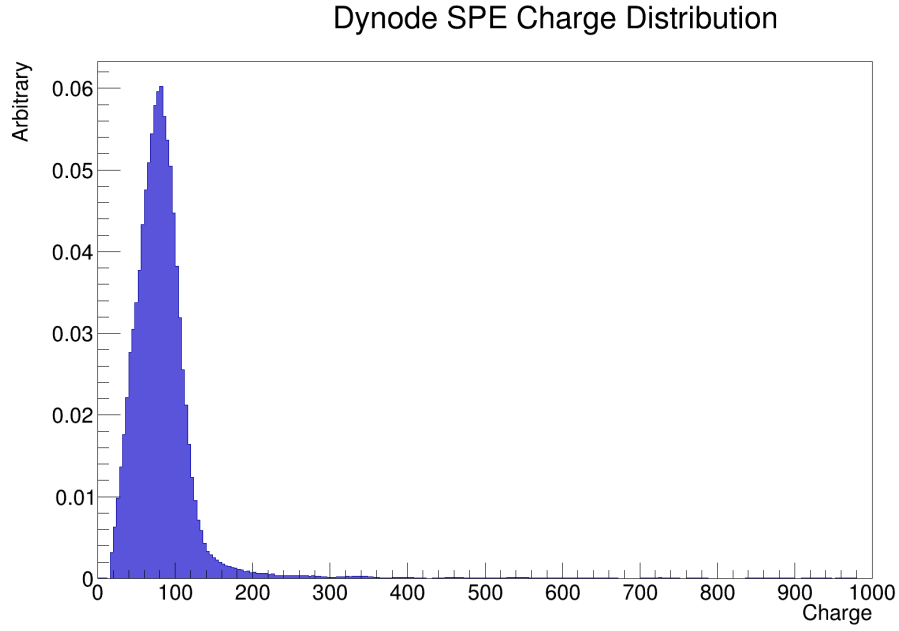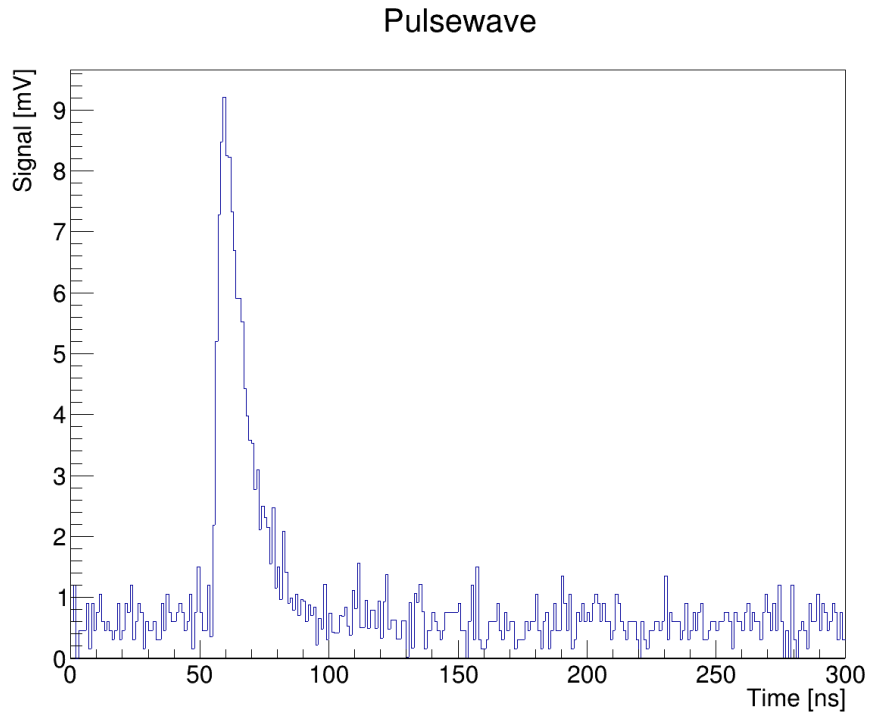
(a) SPE Charge Spectrum of the dynode PMTs.
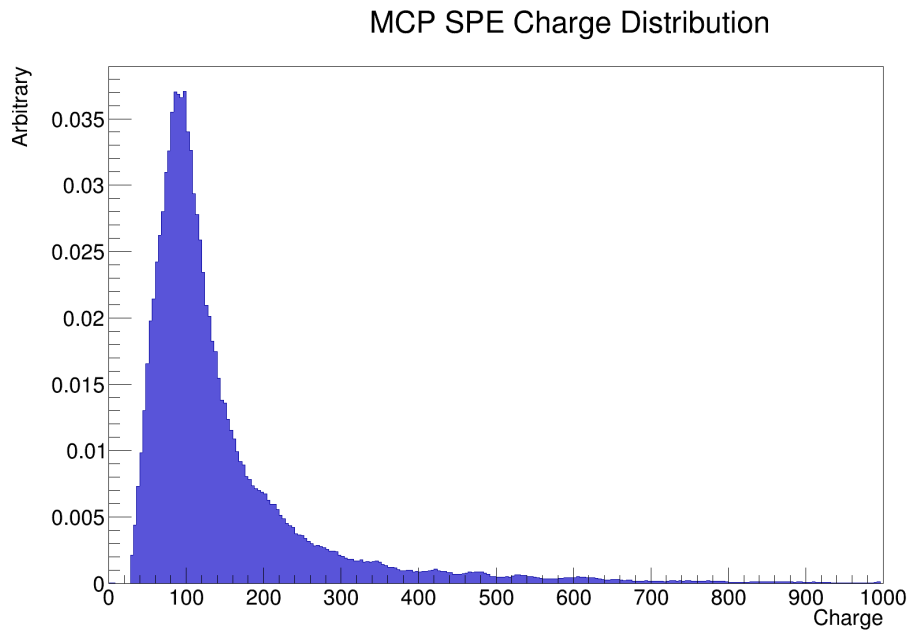
(b) SPE Charge Spectrum of the MCP PMTs.
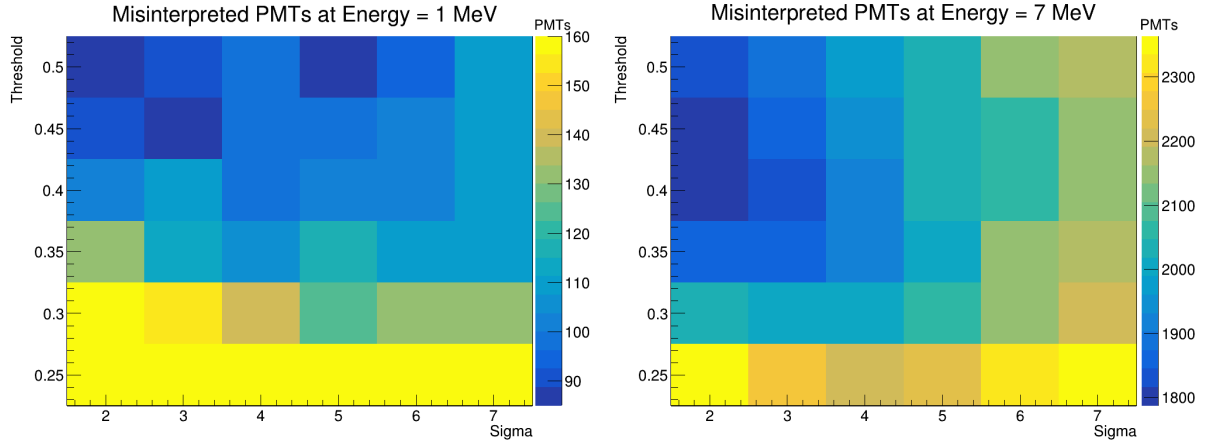
Figure 3.8: The smoothed SPE Charge Distributions.
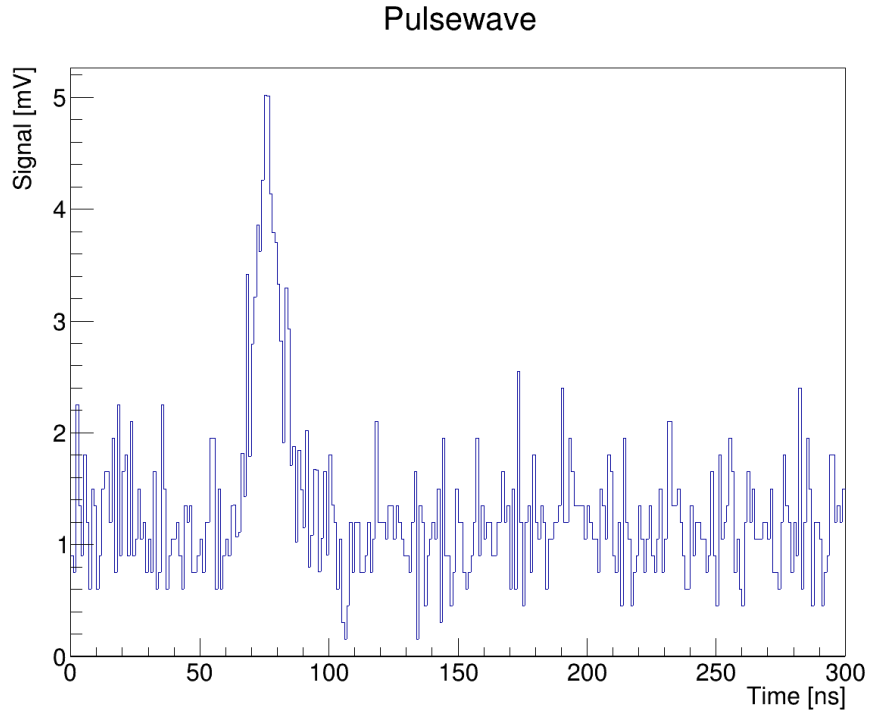
(a) SPE Pulse Wave at Dynode PMT. A low amplitude and medium noise is present in this frame.

(b) SPE Pulse Wave at MCP PMT. Low noise and a high amplitude is present in this frame.

Figure 3.9: Examples for the simulated SPE Signals. The measured signals displayed in 2.7 are mimicked.

(a) Counting Efficiency at $E = 1\,\mathrm{MeV}$　　　(b) Counting Efficiency at $E = 7\,\mathrm{MeV}$

Figure 3.10: Comparison of the Performance of Different TSpectrum Parameters. The average number of misinterpreted PMTs (meaning $n_{PE,PC} \neq n_{PE,\mathrm{TRUE}}$) per event is shown.

3.3 Analyzing Signals

3.3.1 Peak Counting

In order to identify peaks at the PMT signal, the ROOT class TSpectrum is used. It was originally created to analyze γ-ray spectra and uses markov chain algorithms to suppress noise and enhance peaks before counting them. The peak searching function requires two parameters: A minimal σ at which a peak is identified as such, and a threshold $0 < \text{threshold} < 1$, which ignores any peak that is smaller than the threshold times the height of the highest peak. The parameters that yield the highest number of correctly identified PMT signals have to be chosen. The challenge is to balance the peak searching in such a way that no noise will be counted, but the identification of multiple PE at a PMT is maximized. For noise cancelling, a cut-off has been implemented that prevents counting a peak that is smaller than $4\,\mathrm{mV}$. Comparing this with the amplitude distribution, $1.8\,\%$ of PE at MCP PMTs will be lost this way. This cutoff is needed to optimize the TSpectrum parameters to also function with higher numbers of PE. The following parameters have been chosen

$$\sigma = 3\,, \quad \text{threshold} = 0.45\,, \tag{3.21}$$

as they yield the minimum number of miscounted PMTs, as seen in figure 3.10. More detailed information on the performance of peak searching at the chosen parameters is given in figure 3.11. At 1 MeV, 0.31 % of PMTs are misinterpreted compared to 5.03 % at 7 MeV, considering a distance to the center of the CD of 800 cm.
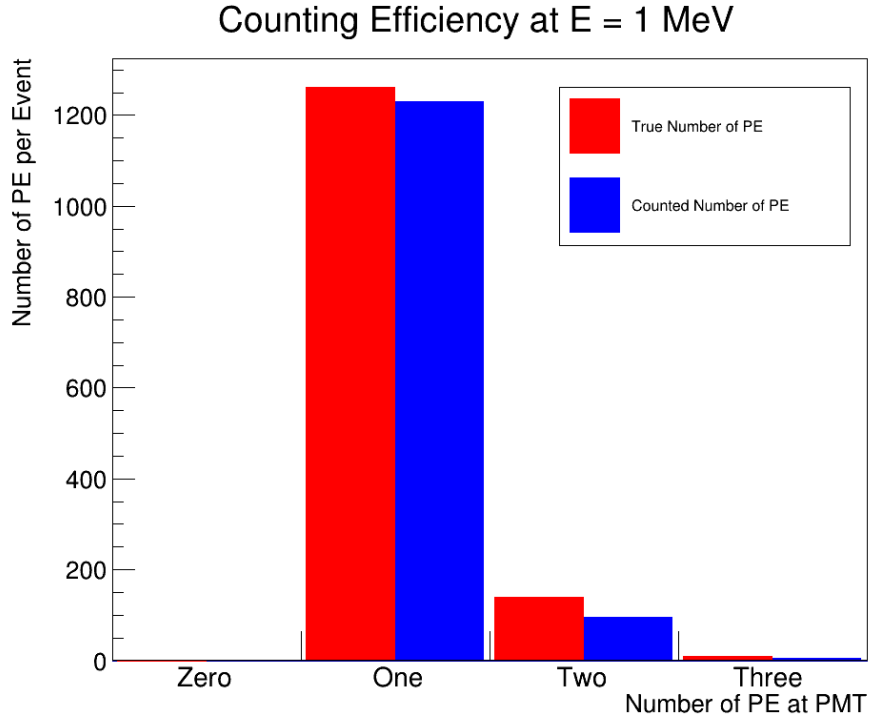
(a) Counting Performance at $E = 1\,\mathrm{MeV}$
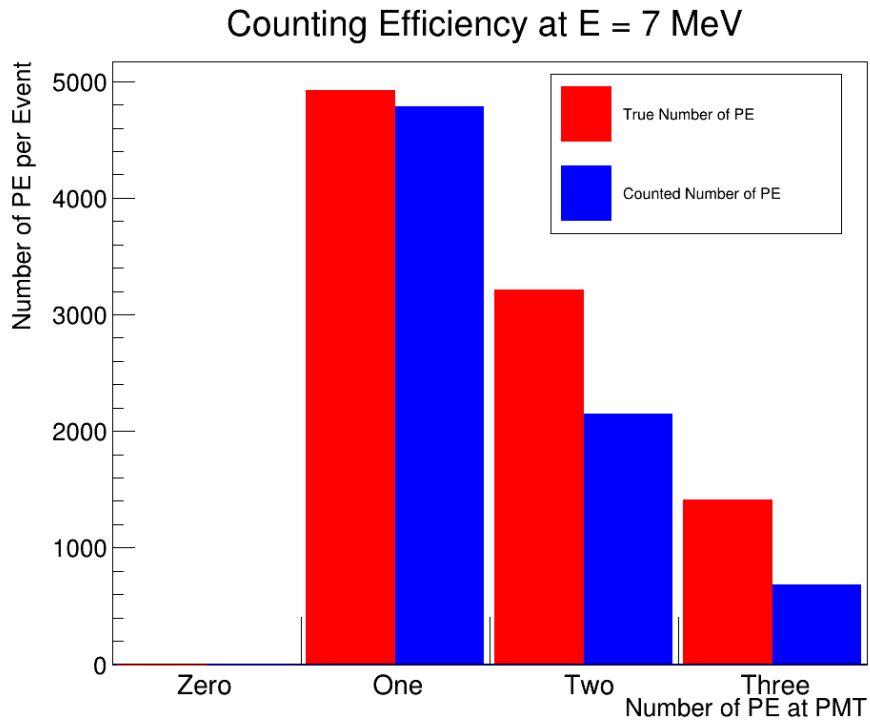
(b) Counting Performance at $E = 7\,\mathrm{MeV}$

Figure 3.11: The Counting Performance for the Chosen Parameters. One can see the importance of identification of multiple hits at higher energies, but also the decreasing success in analyzing PMTs succesfully.

3.3.2 Charge Integration

To retrieve the area beneath the pulse wave at each PMT, the integral is needed. There-fore, the content of each of the 300 bins is summed. To eliminate the positive contribution of the noise, a baseline value is subtracted from that sum. The baseline is constructed by summing the last 75 bins, which do not contain pulse waves. The average bin content in that area is multiplied by 300 and subtracted from the integral of the entire frame. The measured charge $\hat{Q}_i$ at PMT i is therefore calculated via

$$\hat{Q}_i = \sum_{j=1}^{300} C_j - \frac{300}{75} \sum_{j=225}^{300} C_j \,, \tag{3.22}$$

where C_j is the height of bin j. These values will be summed separately for each PMT type. To retrieve an estimation for the number of PE $\hat{N}_{PE}$, the sum for each PMT type is divided by the mean of the respective SPE charge distribution shown in section 3.2.4. Then, $\hat{N}_{PE}$ is given by

$$\hat{N}_{PE} = \hat{N}_{PE,\mathrm{MCP}} + \hat{N}_{PE,\mathrm{Dyn}} \,, \tag{3.23}$$

$$\hat{N}_{PE,\mathrm{MCP}} = \frac{1}{\langle Q \rangle_{\mathrm{MCP}}} \cdot \sum_{i,\mathrm{MCP}} \hat{Q}_i \,, \tag{3.24}$$

$$\hat{N}_{PE,\mathrm{Dyn}} = \frac{1}{\langle Q \rangle_{\mathrm{Dyn}}} \cdot \sum_{i,\mathrm{Dyn}} \hat{Q}_i \,. \tag{3.25}$$

This charge analysis yields a systematic error. When no PE is produced (NPE), averagely $\langle q \rangle_{\mathrm{NPE}} \sim 2.7$ are added to the sum of charge to the respective PMT type. Compared to the mean SPE charges

$$\langle Q \rangle_{\mathrm{DYN}} = 85.5 \tag{3.26}$$

$$\langle Q \rangle_{\mathrm{MCP}} = 147.8 \,, \tag{3.27}$$

this yields 3.2% of $\langle Q \rangle_{\mathrm{DYN}}$, and 1.8% of $\langle Q \rangle_{\mathrm{MCP}}$. Considering the case that not a single PE at every PMT would be produced, this method would yield a PE guess of ~ 390. At 1 MeV, $\sim 15{,}000$ PMTs will get no PE signal and the influence of this faulty analysis is large. This is countered with a threshold of $q = 35$ that the analyzed charge needs to surpass in order to be considered in the sum of q_i. Since the NPE and SPE spectra overlap, this threshold is not ideal. The misinterpreted NPE signals are reduced drastically however. The NPE spectrum is shown in figure 3.12.
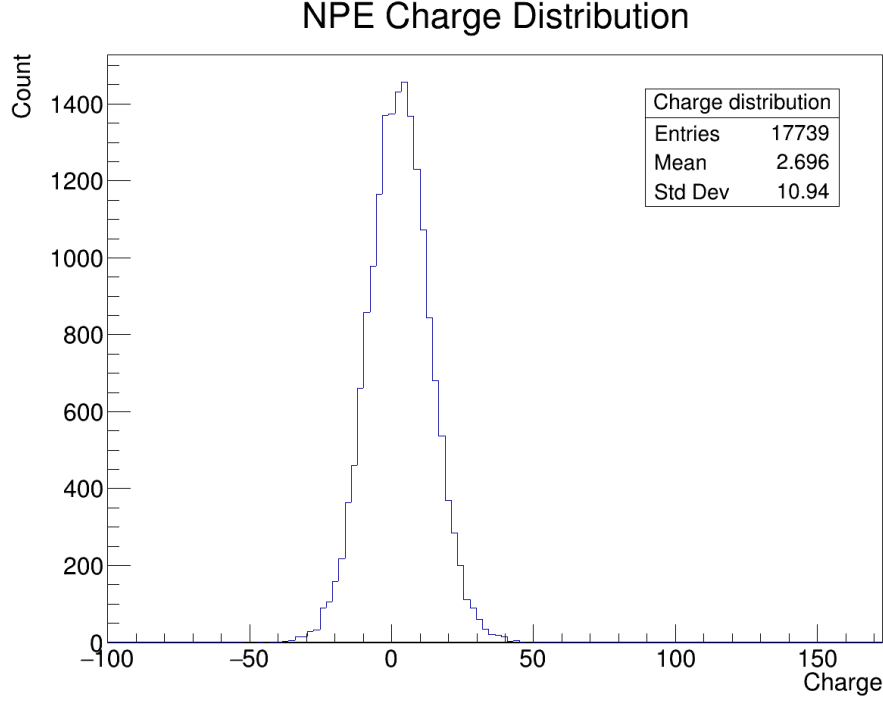
Figure 3.12: The NPE Charge Distribution.

3.4 Energy Reconstruction

An estimation for the energy $\hat{E}$ is given with the knowledge about the mean light yield, local detection efficiency (LDE), location of event in the CD $\vec{R}$, and the estimate for the number of PE. Considering the light yield shown in equation (3.2), $\hat{E}$ is given by

$$\hat{E} = \left(\frac{\hat{N}_{PE}}{\text{LDE}(\vec{R})} + 752 \right) \div 13137 \,. \tag{3.28}$$

The LDE denotes the possibility of a photon emitted at location $\vec{R}$ to produce a PE. It is calculated in the TMC by summing up the LUT values of each PMT while creating the PMT signals

$$\text{LDE}(\vec{R}) = \sum_i \text{LUT}(d_i, \theta_i) \,, \tag{3.29}$$

with d and θ as in equation (3.7). The LDE is shown in figure 3.13. As mentioned in section 2.5, an offset for the energy estimate by peak counting $\hat{E}_{PC}$ is expected, increasing with the true number of PE N_{PE}. Especially because $\hat{E}_{PC}$ is used for the likelihood method which will be explained shortly, this offset should be calibrated. Considering the offset shown in figure 3.14, the fit with the linear function

$$\frac{\hat{E}_{PC}}{E_{\text{True}}} = b \cdot E_{\text{True}} + c \tag{3.30}$$
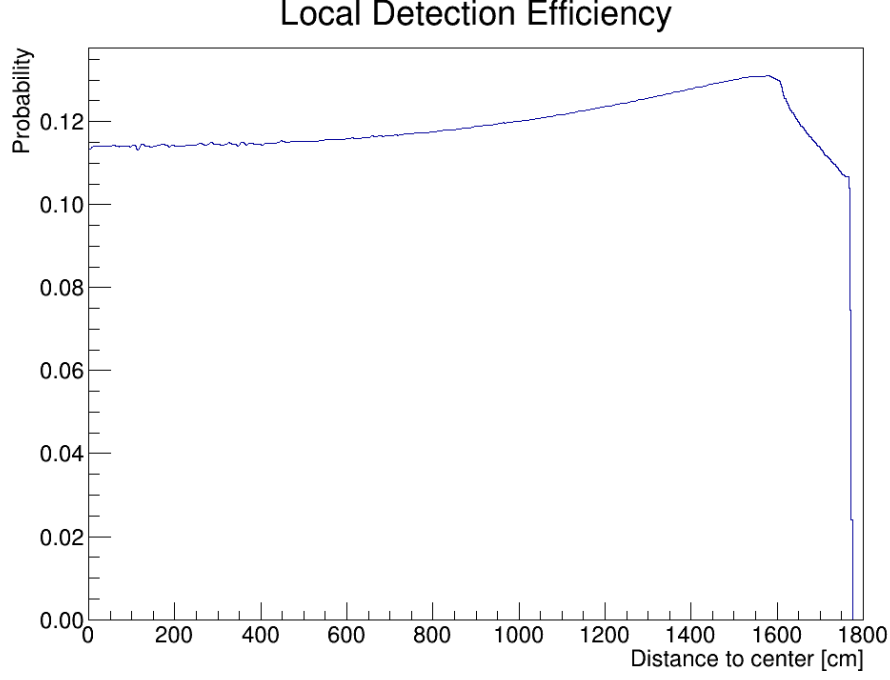
Figure 3.13: The LDE of JUNO dependent on the distance to the center of the CD, calculated with data from the JUNO simulation used to create the LUT.

Table 3.1: The Parameters used to calibrate the offset.

Distance to Center [cm]	b	c
0	0.02046 ± 0.00395	0.9651 ± 0.0297
800	0.02326 ± 0.00260	0.9911 ± 0.0146
1650	0.03491 ± 0.00298	0.7852 ± 0.0212

yields the parameters shown in table 3.1. At $d = 1650$, a systematic error is expected, as the decrease of $\hat{E}/E_{\text{TRUE}}$ deviates from its linear shape. This problem could not yet have been resolved and simulation at the edge of the detector yield unreliable results. The calibrated energy estimate $\hat{E}_{\text{Correct}}$ of $\hat{E}_{PC}$ is then given by

$$\hat{E}_{\text{Correct}} = \frac{c - \sqrt{c^2 - 4 \cdot b \cdot \hat{E}_{PC}}}{2b} \, . \tag{3.31}$$

Likelihood Method

The calibrated energy estimate by peak counting $\hat{E}_{PC}$ is used as first energy guess in the likelihood method. Similar to the loop where PEs are created, this energy guess is used to estimate the number of emitted photons

$$\hat{N}_{EM} = 13137 \cdot \hat{E}_{PC} - 752 \, . \tag{3.32}$$
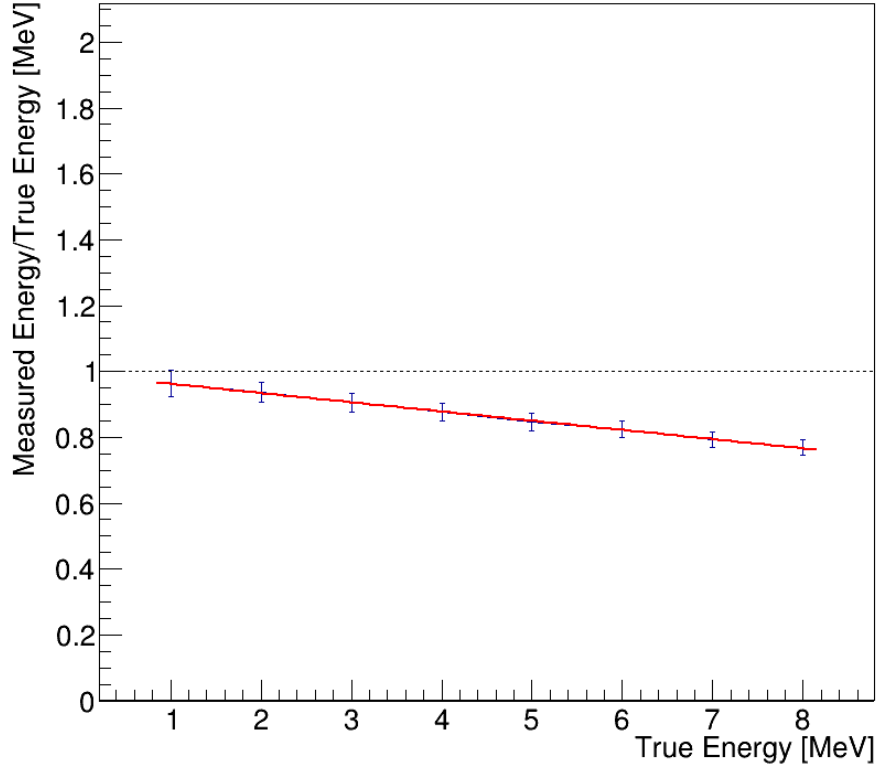
43

Energy with Counting Method

Figure 3.14: The Decrease of $\hat{E}_{PC}/E_{\text{True}}$ at a distance to the center of the CD of 800 cm.

To regain a new estimation for $\hat{N}_{PE}$, a loop over all PMTs is needed similar to the creation of events explained in the previous sections. The following calculations will be made for every PMT. The PE expectation is calculated with

$$\langle n \rangle = \hat{N}_{PE} \cdot \text{LUT}(d, \theta) \tag{3.33}$$

as in section 3.2. $\langle n \rangle$ is used to create a Poisson distribution $P_{\langle n \rangle}(x)$. Now, the charge distributions for different number of PE Q_n at a single PMT are needed. These are created from the SPE charge distribution Q_1 shown in section 3.2.4 by combination

$$Q_n(x) = \sum_{y+z=x} Q_1(y) \cdot Q_{n-1}(z) \,. \tag{3.34}$$

The NPE spectrum is extracted from the simulation with $N_{EM} = 0$. In this TMC, up to three PE are considered in the likelihood method. The resulting charge distributions are shown in figure 3.15. The Q_n are further normalized and then scaled with the probability of n PE according to the Poisson distribution

$$Q'_n = P_{\langle n \rangle}(n) \cdot Q_n \,. \tag{3.35}$$

44
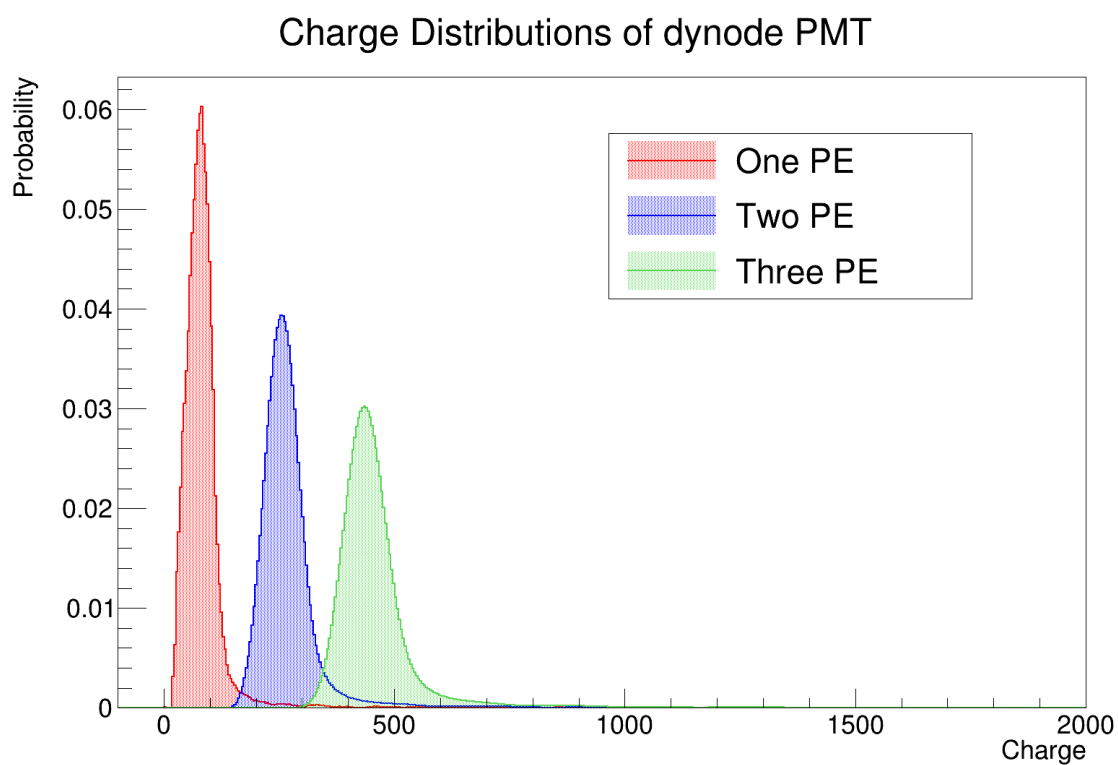
(a) The Charge Distribution at dynode PMTs
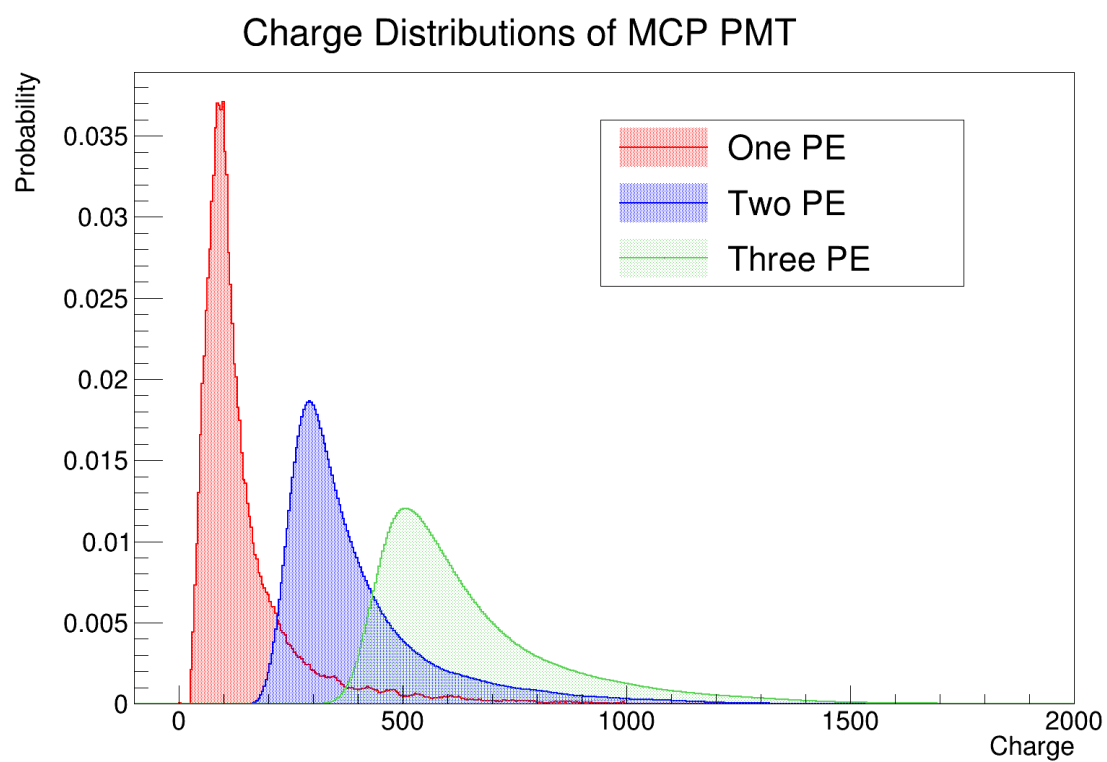
(b) The Charge Distribution at MCP PMTs

Figure 3.15: The Charge distributions at different numbers of PE. The distributions over-
lap heavily for MCP PMTs

Evaluating the height I_n of Q'_n at the charge q measured for that PMT yields the relative probability of n PE

$$I_n = Q'_n(q) \,. \tag{3.36}$$

The probability P_N for N PE is given by

$$P_N = \frac{I_N}{\sum_n I_n} \,. \tag{3.37}$$

The new estimation for the number of PE at the PMT $\hat{n}_{PE}$ is

$$\hat{n}_{PE} = \sum_{N=1} N \cdot P_N \,. \tag{3.38}$$

This calculation is done for every PMT i and the $\hat{n}_{PE,i}$ are summed up for the estimation of total PE

$$\hat{N}_{PE,L} = \sum_i \hat{n}_{PE,i} \,. \tag{3.39}$$

With $\hat{N}_{PE,L}$, the new energy estimate E_L can be calculated.

3.5 Output

Along with the energy estimations by peak counting, charge integration and likelihood method (E_{PC}, E_{CI}, E_L) the optimal energy estimation E_O is calculated for each event. E_O mimics perfect peak counting and is calculated with $N_{PE,\text{True}}$. An event at given energy E_{True} is repeated and the energy estimates recorded seperately. For each E_{True} and each method, a gaussian is fitted to the distribution. The mean $\langle E \rangle$, sigma $\sigma_{E,0}$ and the uncertainty of sigma of the gaussian fit are extracted and examined. Sigma (and its uncertainty in the same way) is converted with the following equation

$$\sigma_E = \frac{\sigma_{E,0}}{\langle E \rangle} \cdot 100 \tag{3.40}$$

and yields the energy resolution in percent.

3.6 Factors Not Implemented

In the scope of this thesis, some factors have been ignored. In order to evaluate the results properly, some aspects that have not been mentioned in chapter 3 yet will be listed here.

Dark Count, Pre- and Afterpulses are neglected. In the TMC, only the calculated PE will trigger a pulse. The spontanious, delayed or premature signals by secondary effects

are not implemented. In reality these will reduce the certainty of the estimate for N_{PE}. Current tests show a dark count rate of 15.3 kHz for dynode PMTs, and 46 kHz for MCP PMTs. This roughly yields a probability of 1.4 % of a spontanious signal within the frame of 300 ns for each MCP-PMT, and 0.45 % for each dynode PMT. Pre-pulses yield faulty time information, however, as the time distribution spreads they improve the possibility of two PE signals to be counted sperately. An after pulse together with its main pulse can wrongly be identified as two photon hits.

The influence of the photons speed on time distribution is neglected. The speed of the photon through the CD is dependent on the photons wavelength. Considering the relevant wavelengths and JUNOs diameter of 35 m, the maximum time spread is $\sim 2\,\mathrm{ns}$.

A large influence not covered in this TMC is the influence of photon scattering on the time distribution. With the attenuation length $L = 20\,\mathrm{m}$, around $e^{\frac{17.7}{L}} \approx 41\,\%$ of photons created at the center of the CD will have been scattered upon reaching a PMT. The longer photon track can yield a delay up to the range of μs. Although applying this effect is not trivial, the time spread will decrease the probability of overlapping PE signals significantly and therefore improve the performance of PC, presuming all scattered photons can be matched with the event.

However, the factors implemented in the TMC are sufficient enough to gain information on the influence of charge distribution on energy resolution and the performance of the likelihood method. Considering dark count, pre- and after-pulse and photon scattering in the TMC requires a good strategy concerning vetoing afterpulses while not ignoring scattered light and opens up a different topic on how to classify PE signals which is outside the scope of this thesis.

4 Results

In this chapter, results regarding the energy resolution are presented and discussed. For reference and first analysis, simulations at the center of the CD are presented first in section 4.1. To analyse the influence of the charge spectrum, the same simulation is repeated with modified charge distributions, which is presented in section 4.2.

4.1 Center of the CD

The position has been set to the absolute center of the CD. As the statistics of the LUT at the center of the CD is sufficent, the threshold for the angle in the LUT has been turned off for this simulation. 7,000 events have been simulated for every energy in the range of 1 to 9 MeV in steps of 2 MeV. The resulting energy estimations can be seen in figure 4.1. One immidiately notices the offset for $\hat{E}_L$. This is explained with the fact that only up to three PE are implemented in the likelihood method. Considering a 4 PE signal at a PMT, the measured charge would most likely be in the area where the four PE spectra peaks. With the likelihood method as it is, only the tails of the other multi-PE charge distribution are in that range. Without the large weight the four PE spectrum would have, the likelihood method estimates a value in the range of 2-3 PE. Thus, for every PMT with 4 PEs, the likelihood method estimates more than 1 PE less. The energy resolution is given in figure 4.2. The resolution shows the expected curve $\propto 1/\sqrt{E}$. Ecept for CI, all methods show a resolution better than 3% at 1 MeV. However, the TMC is not able to prognose if JUNO will reach this target, since many aspects of JUNO are not implemented in the TMC and the absolute values of energy resolution are not conclusive enough. The expected shape and range of the energy resolution indicates however, that no coarse mistake has been made that reflects onto the energy resolution. The values of the energy resolution are displayed in table 4.1.
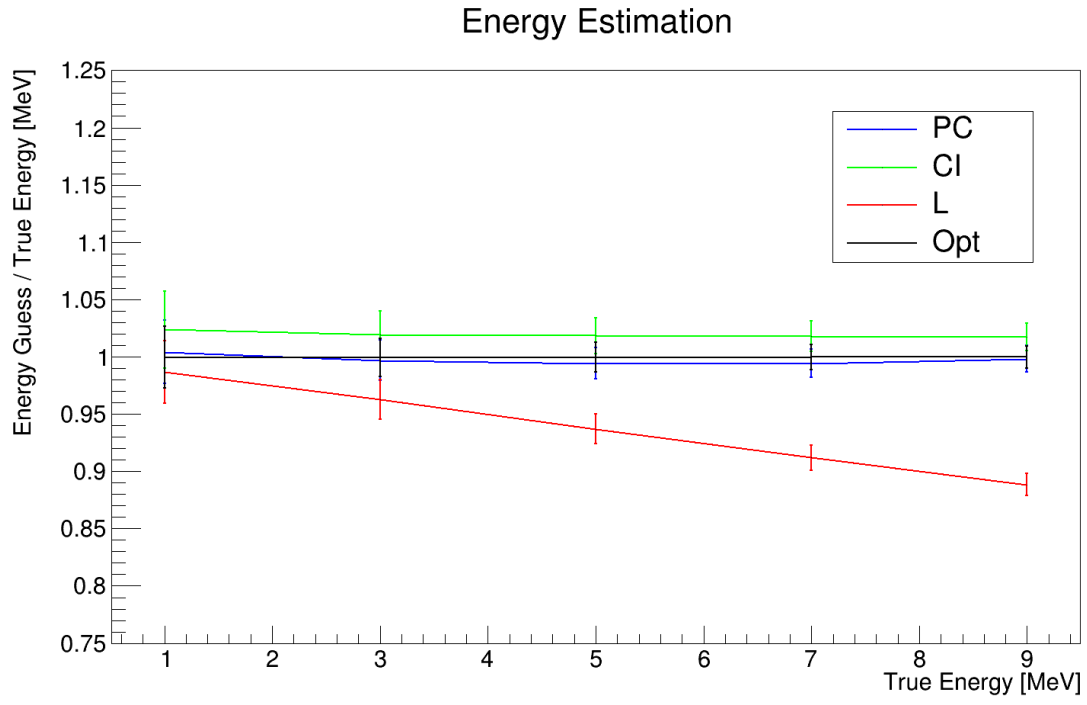
Figure 4.1: The energy estimation at the center of the CD. The error is the energy reso-
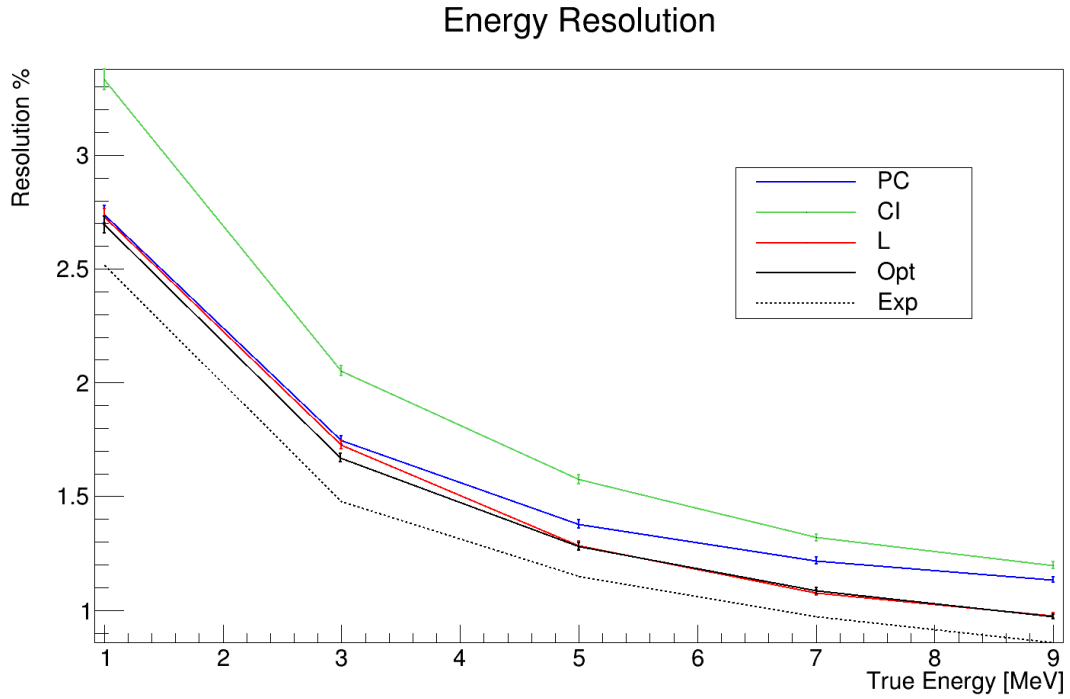lution shown in figure 4.1.

Figure 4.2: The energy resolution at the center of the CD. The error is the uncertainty of
the gauss fit.

Table 4.1: Values for energy resolution at the center of the CD. The fitting error mainly depends on the number of events = 7,000.

E [MeV]	Method	σ [%]
1	PC	2.74 ± 0.04
	CI	3.33 ± 0.04
	L	2.73 ± 0.04
	Opt	2.69 ± 0.04
3	PC	1.75 ± 0.02
	CI	2.05 ± 0.02
	L	1.73 ± 0.02
	Opt	1.67 ± 0.02
5	PC	1.38 ± 0.02
	CI	1.57 ± 0.02
	L	1.28 ± 0.02
	Opt	1.28 ± 0.02
7	PC	1.22 ± 0.01
	CI	1.32 ± 0.02
	L	1.08 ± 0.01
	Opt	1.09 ± 0.01
9	PC	1.13 ± 0.01
	CI	1.20 ± 0.01
	L	0.99 ± 0.01
	Opt	0.97 ± 0.01

Table 4.2: The differences in energy resolution. The error is $\sqrt{\Delta\sigma_1^2 + \Delta\sigma_2^2}$, assuming Gaussian error propagation.

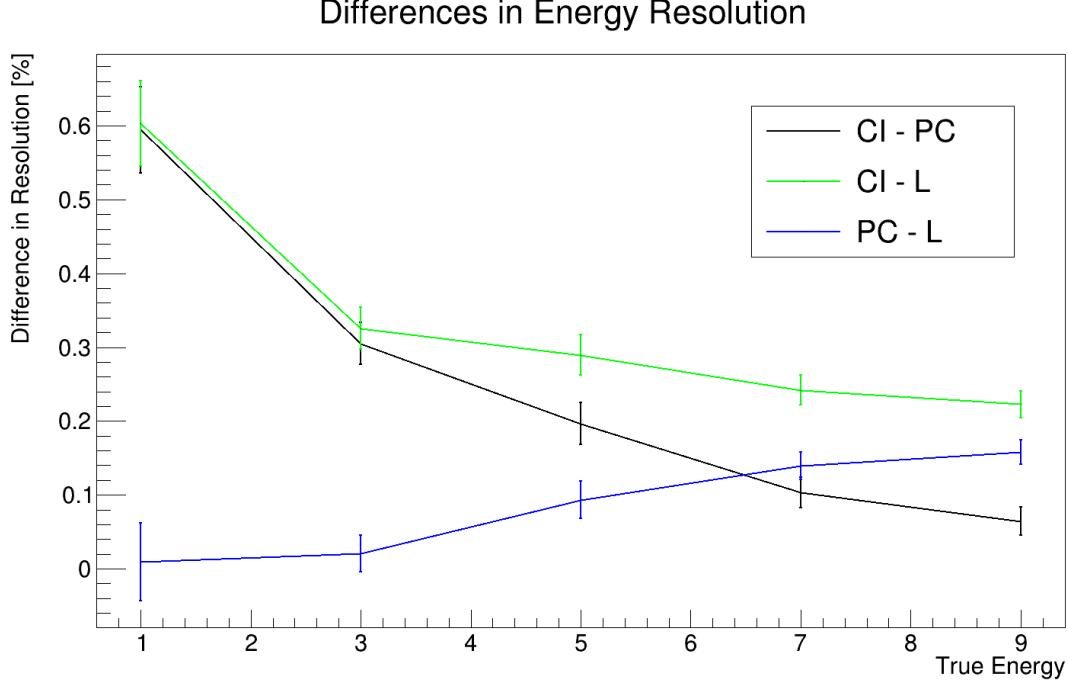| E_{TRUE} [MeV]	Methods	
1	$\sigma_{CI} - \sigma_{PC}$	0.56 ± 0.06
	$\sigma_{CI} - \sigma_L$	0.60 ± 0.06
	$\sigma_{PC} - \sigma_L$	0.01 ± 0.05
3	$\sigma_{CI} - \sigma_{PC}$	0.30 ± 0.03
	$\sigma_{CI} - \sigma_L$	0.33 ± 0.03
	$\sigma_{PC} - \sigma_L$	0.02 ± 0.03
5	$\sigma_{CI} - \sigma_{PC}$	0.20 ± 0.03
	$\sigma_{CI} - \sigma_L$	0.29 ± 0.03
	$\sigma_{PC} - \sigma_L$	0.09 ± 0.03
7	$\sigma_{CI} - \sigma_{PC}$	0.10 ± 0.02
	$\sigma_{CI} - \sigma_L$	0.24 ± 0.02
	$\sigma_{PC} - \sigma_L$	0.14 ± 0.02
9	$\sigma_{CI} - \sigma_{PC}$	0.06 ± 0.02
	$\sigma_{CI} - \sigma_L$	0.22 ± 0.02
	$\sigma_{PC} - \sigma_L$	0.16 ± 0.02

Figure 4.3: The differences of energy resolution values. A positive value of $\sigma_1 - \sigma_2$ indicates superior resolution with method 2.

The shown 'expected resolution' is calculated with

$$\sigma_{\text{Exp}} = \frac{1}{\sqrt{\langle N_{EM} \rangle (E)}}, \tag{4.1}$$

with the $\langle N_{EM} \rangle$ used in the TMC. This value only considers statistical fluctuation of $\langle N_{EM} \rangle$ since $\sigma_{EM} = \sqrt{\langle N_{EM} \rangle}$. Since statistical fluctuation of the resulting PE and the detection of PE is ignored, it naturally yields the best resolution. The shown 'optimal resolution' is calculated with full knowledge on $N_{PE,\text{TRUE}}$. The difference to 'expected resolution' therefore displays the influence of the fluctuation of resulting PE at the PMT. The energy resolution of PC and CI contains additional influences depending on the detection efficiency. As expected, CI yields the lowest resolution. The shape is extremely similar to the aforementioned artificial resolutions. This indicates that the detection efficiency is not energy dependent. This is expected, as overlapping signals do not pose a problem when summing up the area beneath the pulse waves. This is opposed to PC which yields a reliable identification of PE at low energies and is thus near 'optimal resolution'. As the energy increases, the information loss increases and at 9 MeV, $\sigma_{PC} \to \sigma_{CI}$. The likelihood method improves the energy resolution through the entire energy range. At low energies, $\sigma_L \approx \sigma_{PC}$, and at high energies $\sigma_L \approx \sigma_{\text{Opt}}$. The differences of σ_{PC}, σ_{CI} and σ_L are displayed in figure 4.3. The values for these differences are displayed in table 4.2. At 1 MeV, the PC and L yield a σ 0.6% lower than that of CI, which is a relative improvement

of

$$\frac{\sigma_{CI} - \sigma_L}{\sigma_{CI}} = \frac{0.6}{3.33} \approx 18\% \,. \tag{4.2}$$

As σ_{CI} converges slightly towards σ_{Opt} with increasing energy, the absolute difference to the likelihood method reduces to 0.22% at 9 MeV. With $\sigma_{CI} = 1.20\%$, the relative improvement is still

$$\frac{\sigma_{CI} - \sigma_L}{\sigma_{CI}} = \frac{0.22}{1.20} \approx 18\% \,. \tag{4.3}$$

Considering the non ideal curve in figure 4.2, this is just a rough estimate for the improvement of the likelihood method compared to charge integration method. As the Peak Counting is near perfect at low energies, the likelihood method only shows improvement at higher energies with up to

$$\frac{\sigma_{PC} - \sigma_L}{\sigma_{PC}} = \frac{0.16}{1.13} \approx 14\% \tag{4.4}$$

at 9 MeV.

4.2 Influence of Charge Distribution

In order to analyse the influence of the charge distribution, the simulation is conducted with an artificially good charge distribution, shown in figure 4.4. There is no long tail and no overlapping of mulit-PE spectra. This charge distribution is applied to both PMT-types, all other parameters are identical to the previous simulation. The resulting energy estimations can be seen in figure 4.5. One notices the offset of $\hat{E}_{PC}$. Due to the artificial charge distributions, the pulse waves have larger, more uniform amplitudes. This improves the efficiency of the peak finder. As the calibration of $\hat{E}_{PC}$ has not been altered for this simulation, the offset occurs. The energy resolution can be seen in figure 4.6. One immediately notices the improved performance of the CI method. With the artificial charge distribution, the $\hat{N}_{PE}$ is near perfect and the CI energy resolution is near the 'optimal resolution'. The resolution of the likelihood method seems better than the resolution with full knowledge on $N_{PE,\text{TRUE}}$, however this is due to the maximum of three PE considered. With the distinct charge distributions and no overlap, the likelihood method should almost always yield $\hat{n}_{PE} = \hat{n}_{PE,\text{TRUE}}$. Exceptions are the rare cases where noise causes the measured charge to be just outside of the charge spectra and the likelihood method yields $\hat{n}_{PE} = 0$. It also yields 0 in 100% of the cases where more than three PE were produced, which is a loss of roughly $\sim 5\%$ PE at 9 MeV. Therefore, the offset can be explained and the consistency of ignoring these multiple hits results in the energy resolution that is better than 'optimal'. If the likelihood method is equipped with the ability to identify a higher number of hits, one expects the resolution to be 'optimal' as well.
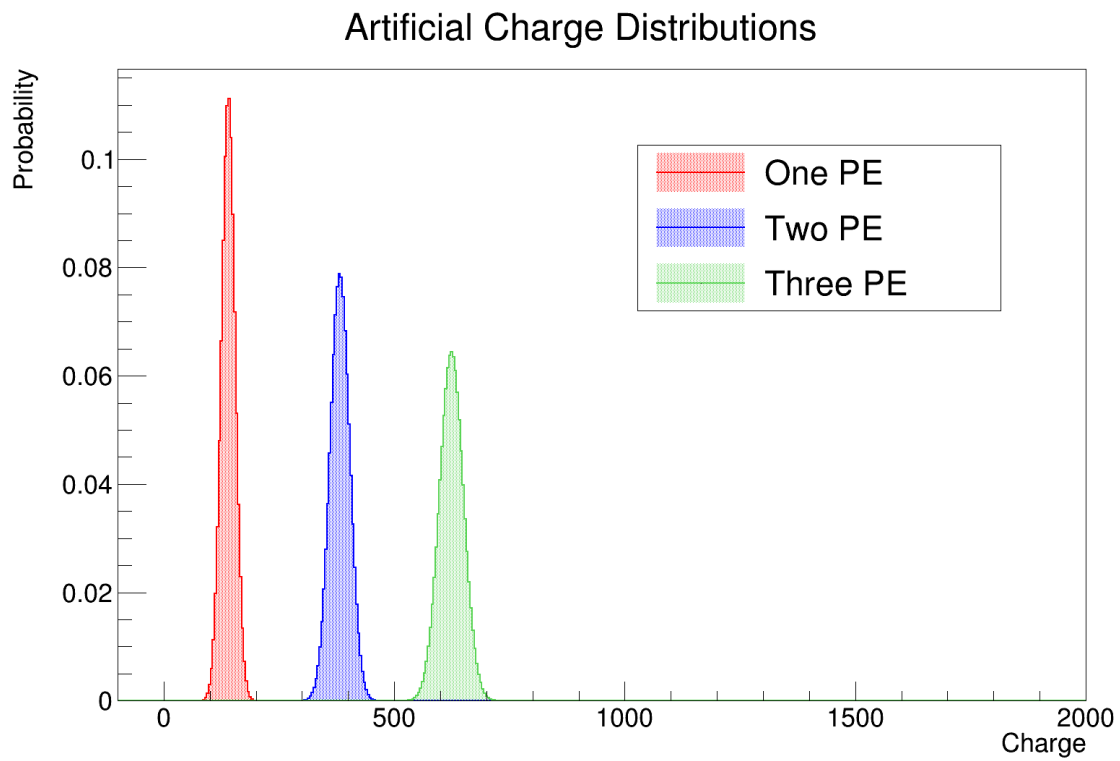
Figure 4.4: The artificial charge distribution. There is no overlap and the spread is very small.
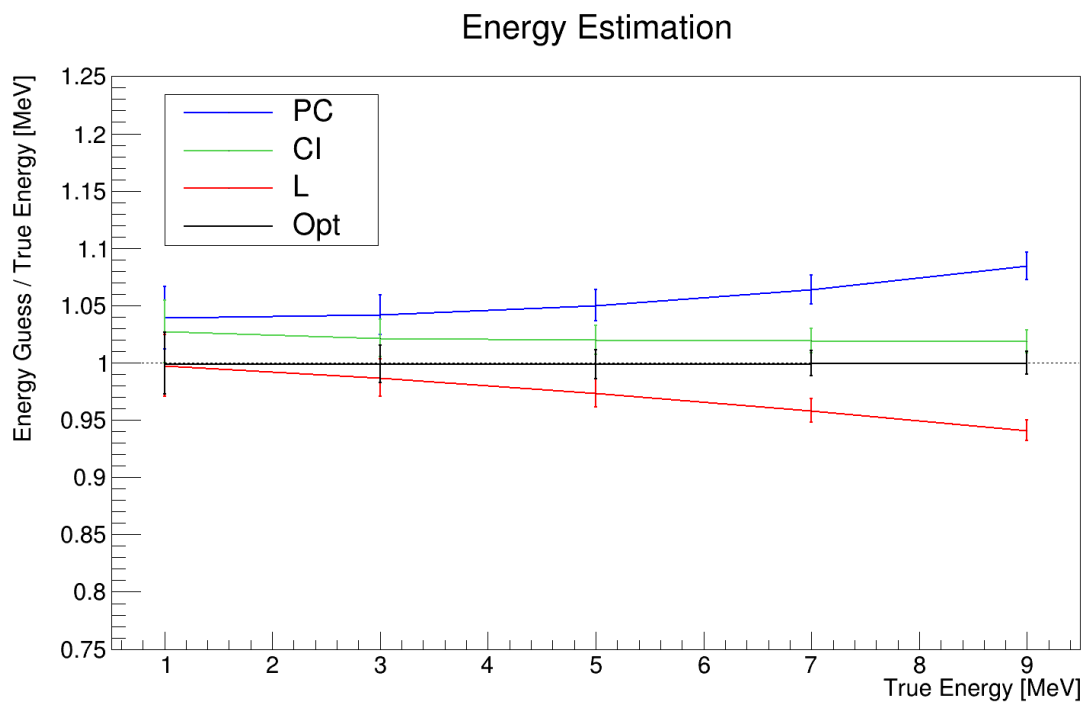

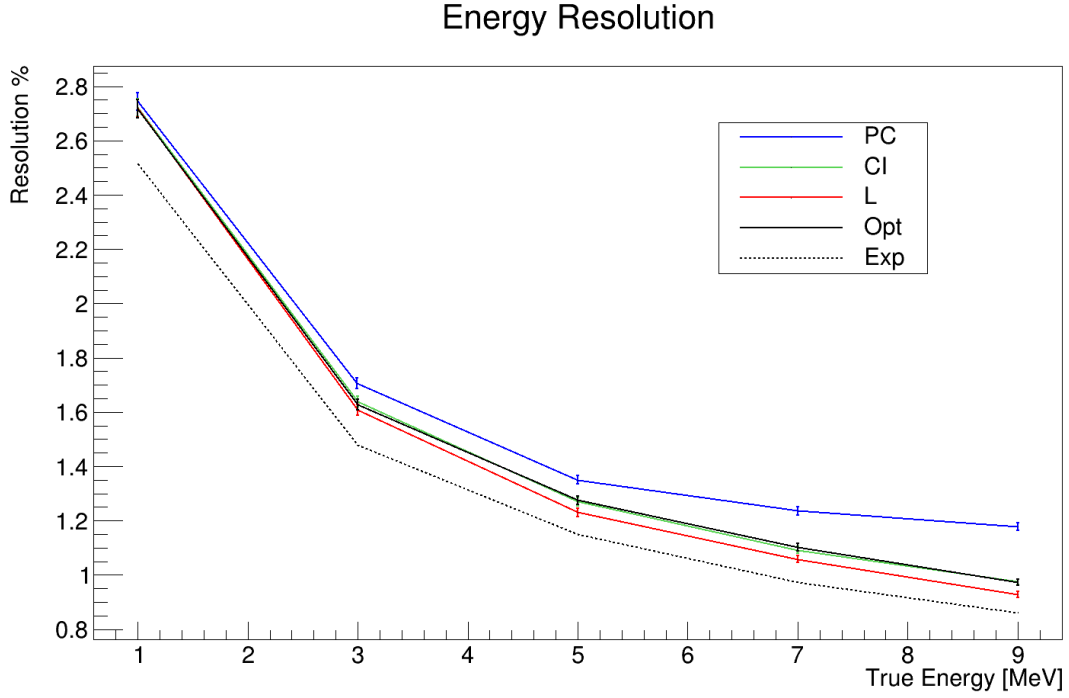Figure 4.5: Energy estimation with artificial charge distribution

Figure 4.6: Energy Resolution with artificial charge distribution

To analyse the influence of the long tail of the charge distribution, the artificial distribution is replaced with the original charge distribution, but where the long tail has been cut off. The resulting spectra are shown in 4.7. The position of the cut was chosen in order to allow slight overlapping of multi-PE spectra. The results of energy resolution are shown in figure 4.8 Although the energy resolution of CI method is not 'optimal' anymore, it is still better than with the original spectrum. Detailed numbers on the energy resolution is given in table 4.3 and the differences are given in table 4.4.
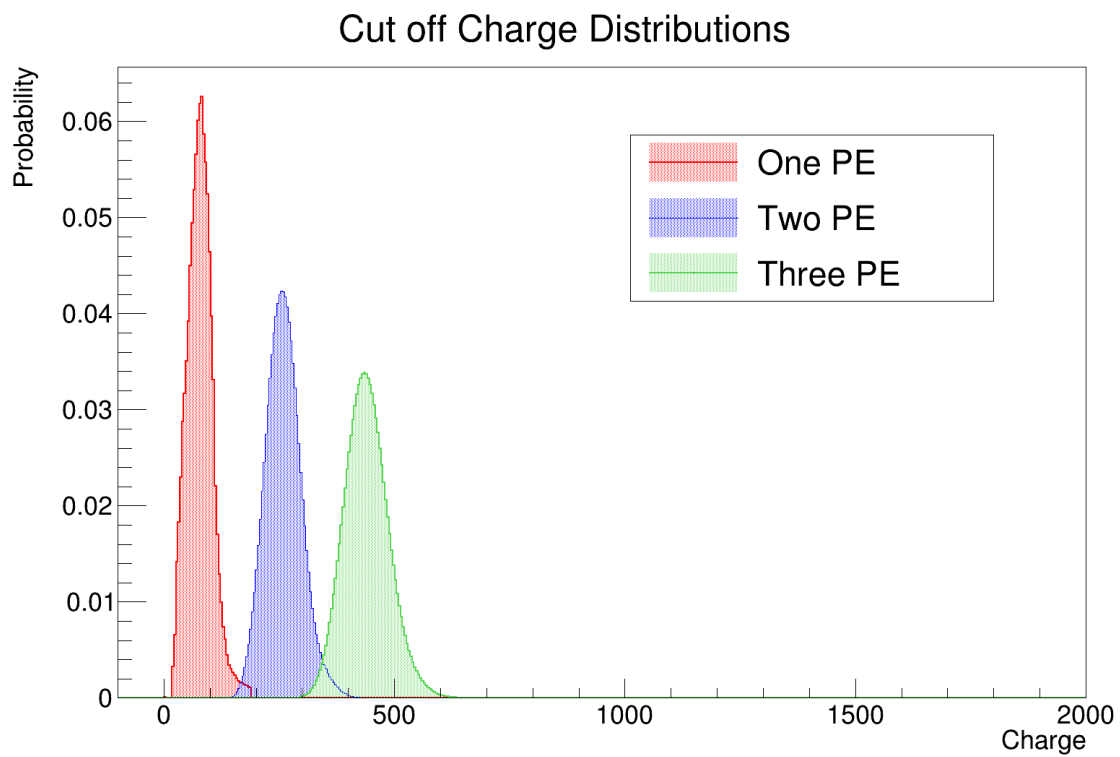
Figure 4.7: The charge spectra Without the long tail
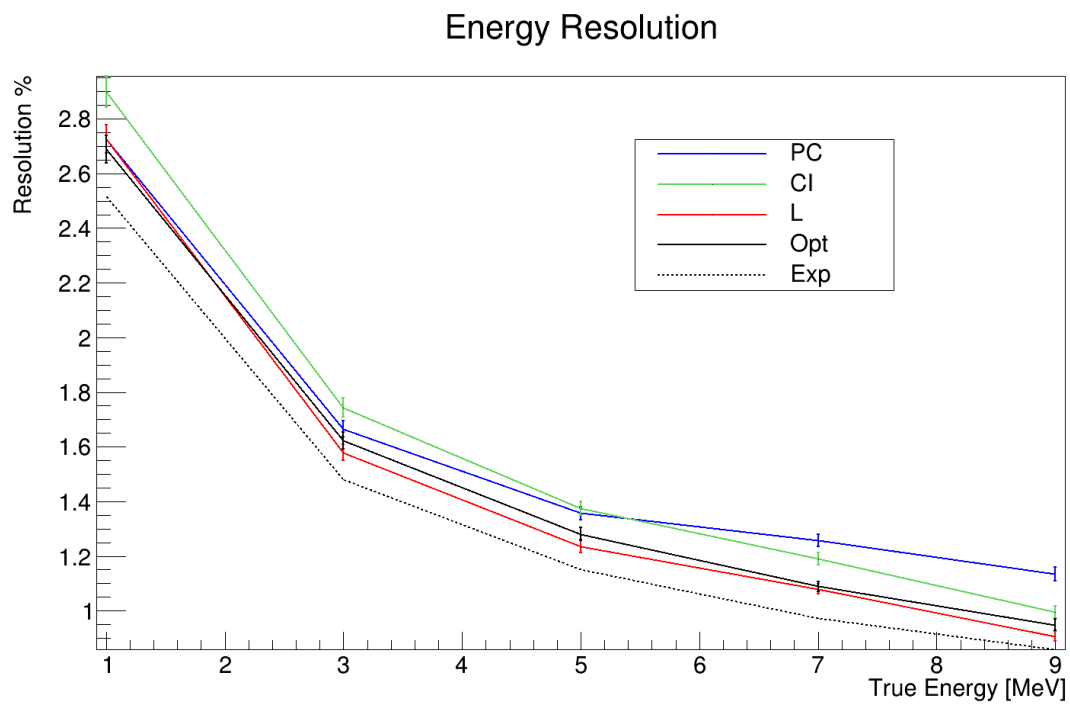
Figure 4.8: Energy eesolution with cut off charge distribution

Table 4.3: σ_{CI} with different charge distributions

E_{TRUE} [MeV]	Charge Distribution		
	Original	Cut Off	Artificial
1	3.33 ± 0.04	2.90 ± 0.06	2.72 ± 0.03
3	2.05 ± 0.02	1.74 ± 0.03	1.64 ± 0.02
5	1.57 ± 0.02	1.37 ± 0.03	1.27 ± 0.02
7	1.32 ± 0.02	1.19 ± 0.02	1.09 ± 0.01
9	1.20 ± 0.01	1.00 ± 0.02	0.97 ± 0.01

Table 4.4: The difference of σ_{CI} with different charge distributions

E_{TRUE} [MeV]	Charge Distribution		
	Original - Cut Off	Original - Artificial	Cut Off - Artificial
1	0.43 ± 0.07	0.61 ± 0.05	0.18 ± 0.07
3	0.31 ± 0.04	0.41 ± 0.03	0.11 ± 0.04
5	0.20 ± 0.03	0.30 ± 0.03	0.10 ± 0.03
7	0.13 ± 0.03	0.23 ± 0.02	0.10 ± 0.02
9	0.20 ± 0.03	0.22 ± 0.02	0.02 ± 0.02

The results indicate, that the major influence on the bad energy resolution with the *CI*-method is in fact the elongated tail of the charge distribution. Removing the tail yields an improved resolution at $\sim 0.4\,\%$ less than with tail at 1 MeV, a relative improvement of

$$\frac{\sigma_{CI,\text{Original}} - \sigma_{CI,\text{CutOff}}}{\sigma_{CI,\text{Original}}} = \frac{0.43}{3.33} \approx 13\,\% \,. \tag{4.5}$$

Although the cut off charge spectrum is still broad and the multi-PE spectra overlap slightly, $\sigma_{CI,\text{CutOff}}$ yields nearly optimal resolution at 9 MeV. The same distribution with the tail decreases the energy resolution by $0.2\,\%$, which is roughly

$$\frac{\sigma_{CI,\text{Original}} - \sigma_{CI,\text{CutOff}}}{\sigma_{CI,\text{Original}}} = \frac{0.20}{1.20} \approx 17\,\% \,. \tag{4.6}$$

5 Conclusion

The TMC was able to yield insights to the influence of the PMT charge spectrum on the energy resolution as well as classify the performance of the likelihood method. Conducting analysis with the TMC was a good choice, as control over key aspects of the JUNO detector that influence the energy resolution was given. It also allowed to simulate JUNO in a basic setup which proved helpful for analysis of the given problems.

The overall expected energy resolution at JUNO was recreated and conclusive patterns were observed. Energy recreation by Charge Integration yielded the overall worst energy resolution with an almost constant difference to the optimal resolution, which is obtained with the true number of PE, since the detection efficiency of Charge Integration is not energy dependent. In contrary to Peak Counting, which is near optimal at 1 MeV and near Charge Integration energy resolution at 9 MeV as it fails to identify every PE when a high number of PE is present.

The likelihood method, which combines the charge at every PMT, a first energy estimation by Peak Counting and knowledge on the detecting efficiency, yielded near optimal energy resolution throughout the simulation.

Testing the simulation with alternatice charge spectra indicated that the long tail of the charge spectrum, which is especially large for the majority of PMTs, is the main contributer to the bad energy resolution of the Charge Integration method. This was seen as the same charge distributions with the tail cut off yielded a signicantly better performance.

Pulse shape analysis could be the next step in order to minimize the poor detection efficiency of Charge Integration and of Peak Counting at high energies. If a correlation of shape of the pulse and the large tail can be found, pulse analysis can help to distinguish a large pulse from a single PE from overlapping signals of two or more PE.

The likelihood method can further be improved, for example if probability based on time distribution is added to the calculation. This would especially be interesting if effects such as dark current, pre- and after-pulse and the influence of photon scattering on the time distribution is implemented.

Erklärung der Urheberschaft

Hiermit bestätige ich, dass die vorliegende Arbeit von mir selbständig verfasst wurde und ich keine anderen als die angegebenen Hilfsmittel – insbesondere keine im Quellenverzeichnis nicht benannten Internet-Quellen – benutzt habe und die Arbeit von mir vorher nicht in einem anderen Prüfungsverfahren eingereicht wurde. Die eingereichte schriftliche Fassung entspricht der auf dem elektronischen Speichermedium. Ich bin damit einverstanden, dass die Bachelorarbeit veröffentlicht wird.

Ort, Datum   Unterschrift

List of Figures

List of Tables

Bibliography

[1]   F. Capozzi et Al. *status of three-neutrino oscillation parameters, circa 2013*. 2014.

[2]   G. Bellini et Al. *Geo-neutrinos*. 2014.

[3]   Soo-Bong Kim et Al. *Reactor Neutrinos*. 2012.

[4]   Teppei Katore et Al. *Neutrino-nucleus cross sections for oscillation experiments*. 2018. URL: `http://inspirehep.net/record/1499876/plots` (visited on 05/19/2019).

[5]   YE Cing-Chen et Al. *Preliminary study of light yield dependence on LAB Liquid Scintillator Composition*. 2015.

[6]   K.A. Olive et Al. (Particle Data Group). *Chinese Physics C38, 090001*. 2014.

[7]   M. Tanabashi et Al. (Particle Data Group). *Phys. Rev. D 98, 030001*. 2018.

[8]   John Bahcall. "The Solar-Neutrino Problem." In: *Scientific American* 262 (1990).

[9]   John F. Beacom. *The Diffuse Supernova Neutrino Background*. 2010.

[10] Christoph Scholz Fran Zetsche Bogdan Povh Klaus Rith. *Teilchen und Kerne*. Springer-Verlag, 2009.

[11] Inter-University Accelerator Center. *Micro Channel Plate detector (MCP)*. 2014. URL: `http://www.iuac.res.in/atmol/~safvan/mridulathesis/node21.html` (visited on 05/30/2019).

[12] Joseph Amato Enrique Galvez Elizabeth Parks Charles Holbrow James Lloyd. *Modern Introductory Physics*. Springer-Verlag, 2010.

[13] JUNO Collaboration. *Groundbreaking at JUNO*. 2015. URL: `http://juno.ihep.cas.cn/PPjuno/201501/t20150112_135044.html` (visited on 05/20/2019).

[14] JUNO Collaboration. *JUNO Conceptual Design Report*. 2015.

[15] Emily Conover. "A High-Energy Neutrino has been traced to its Galactic Birthplace." In: *Sience News* 194 (2018).

[16] Gordon Danby. "Observation of High-Energy Neutrino Reactions and the Existence of Two Kinds of Neutrinos." In: *Physical Review Letters* 9 (1962).

[17] John Ellis. "The Discovery of the Gluon." In: *50 Years of Quarks* (2014).

[18] G.M.Lewis. *Neutrinos*. 1970.

[19] JUNO PMT Intrumentation Group. *PMT Testing Status Report*. 2019.

[20] Neutrinophysik Universität Hamburg. *JUNO on neutrinophysics UHH homepage*. URL: `www.neutrino.uni-hamburg.de/projekte/juno/` (visited on 05/19/2019).

[21] Miao He. *Double Calorimetry System in JUNO*. URL: `http://inspirehep.net/record/1607835/plots` (visited on 05/20/2019).

[22] Shaomin Chen Jingyi Yi Zhe Wang. *A Precise Calculation of Delayed Coincidence Selection Efficiency and Accidental Coincidence Rate*. 2014.

[23] Benedict Kaiser. *Comissioning of a test facility to charaacterize the JUNO PMTs*. 2016.

[24] Shulin Liu. *Optimal Design of MCP Components in 20-inch MCP-PMT for JUNO*. 2018.

[25] Sebastian Lorenz. *Topological Track Reconstruction in Liquid Scintillator and LENA as a Far-Detector in an LBNO Experiment*. Universität Hamburg, 2016.

[26] Lecture Notes by M. Donega and C. Grab for ETH Zürich. *Monte Carlo Methods, Statistical Methods and Analysis Techniques in Experimental Physics*. URL: `http://ihp-lx.ethz.ch/Stamet/lectureNotes/PDFs/ch4.pdf` (visited on 06/01/2019).

[27] Satoshi Ozak. *Report of the 2004 KEK PS External Review Committee*. 2004.

[28] Sen Qian. *The R&D and Mass Production of the 20 Inch MCP-PMT in China*. 2018. URL: `https://indico.cern.ch/event/686555/contributions/2972374/attachments/1682519/2703560/ICHEP2--MCP-PMTs--V3.0.pdf` (visited on 05/30/2019).

[29] Stefan Scherer. *Symmetrien und Gruppen in der Teilchenphysik*. Springer-Verlag, 2016.

[30] Norbert Schmitz. *Neutrinophysik*. Teubner, 1997.

[31] Aldo Serenelli. *Solar models, Neutrinos and Helioseismology*. 2018. URL: `https://indico.cern.ch/event/734467/contributions/3223797/attachments/1768984/2873416/serenelli_iwdms2018.pdf` (visited on 05/28/2019).

[32] Irene Tamborra. *Supernova Neutrinos: Theory*. 2015.

[33] Mark Thomson. *Modern Particle Physics*. Cambridge University Press, 2013.

[34] Teresa Marrodán Undagoitia. *Measurement of Light Emission in Organic Liquid Scintillators and Studies towards the Search for Proton Decay in the future Large-Scale-Detector LENA*. Technische Universität München, 2008.

[35] Yifang Wang. *JUNO Experiment*. 2014. URL: `https://indico.cern.ch/event/303475/contributions/695094/attachments/574604/791314/JUNO-Paris.pdf` (visited on 05/20/2019).

[36]   Mengjiao Xiao. *JUNO Central Detector and its Calibration Strategy*. 2016. URL: https://indico.ihep.ac.cn//event/6156/session/2/contribution/53/material/slides/0.pdf (visited on 05/20/2019).

[37]   Kai Zuber. *Neutrino Physics*. Dresden University, 2012.